EFFICIENT MOM ANALYSIS OF PRINTED STRUCTURES BY UTILIZING CHARACTERISTIC MODES

A THESIS SUBMITTED TO
THE GRADUATE SCHOOL OF NATURAL AND APPLIED SCIENCES
OF
MIDDLE EAST TECHNICAL UNIVERSITY

BY

METEHAN ÇETİN

IN PARTIAL FULFILLMENT OF THE REQUIREMENTS
FOR
THE DEGREE OF MASTER OF SCIENCE
IN
ELECTRICAL AND ELECTRONICS ENGINEERING

SEPTEMBER 2016

Approval of the thesis:

EFFICIENT MOM ANALYSIS OF PRINTED STRUCTURES BY UTILIZING CHARACTERISTIC MODES

submitted by **METEHAN ÇETİN** in partial fulfillment for the degree of **Master of Science in Electrical and Electronics Engineering Department, Middle East Technical University by,**

Prof. Dr. Gülbin Dural Ünver _____
Dean, Graduate School of **Natural and Applied Sciences**

Prof. Dr. Tolga Çiloğlu _____
Head of Department, **Electrical and Electronics Engineering**

Assoc. Prof. Dr. Lale Alatan _____
Supervisor, **Electrical and Electronics Engineering Dept., METU**

Examining Committee Members:

Prof. Dr. S. Sencer Koç
Electrical and Electronics Engineering Dept., METU _____

Assoc. Prof. Dr. Lale Alatan
Electrical and Electronics Engineering Dept., METU _____

Prof. Dr. Gülbin Dural Ünver
Electrical and Electronics Engineering Dept., METU _____

Prof. Dr. Özlem Aydın Çivi
Electrical and Electronics Engineering Dept., METU _____

Assoc. Prof. Dr. Vakur Ertürk
Electrical and Electronics Engineering Dept., Bilkent University _____

Date: 29/09/2016

I hereby declare that all information in this document has been obtained and presented in accordance with academic rules and ethical conduct. I also declare that, as required by these rules and conduct, I have fully cited and referenced all material and results that are not original to this work.

Name, Last Name: Metehan ÇETİN

Signature: _____

ABSTRACT

EFFICIENT MOM ANALYSIS OF PRINTED STRUCTURES BY UTILIZING CHARACTERISTIC MODES

Çetin, Metehan

M.S., Department of Electrical and Electronics Engineering

Supervisor: Assoc. Prof. Dr. Lale Alatan

September 2016, 74 pages

In recent years, the theory of characteristic modes has been widely used for antenna design purposes. This theory provides physical insight about scattering and radiating properties of conducting bodies. In this thesis work, a MATLAB code is developed for analyzing printed structures by using characteristic mode theory. Characteristic modes of printed structures can be calculated by using the Method of Moments (MoM) matrix corresponding to the structure. To generate the MoM matrix, the electric field integral equation is discretized by using Rao Wilton Glisson (RWG) basis functions and Galerkin's testing procedure. First, characteristic mode analysis of an ultra wide band planar bevel-shaped quasi-monopole antenna structure is made by using the developed code. The results are compared with the results obtained from a commercially available electromagnetic simulation software called FEKO. After verifying the accuracy of the developed code with this comparison, the code is extended to include the analysis of antennas printed on dielectric substrates. For this purpose, discrete complex image method is utilized to obtain the spatial domain Green's functions in layered media. The analysis of rectangular microstrip antennas are performed by using the developed code and the results are compared with FEKO.

Keywords: Characteristic modes, method of moments, numerical analysis, printed antennas, input impedance.

ÖZ

KARAKTERİSTİK MODLAR KULLANARAK BASKILI YAPILARIN VERİMLİ MOM ANALİZİ

Çetin, Metehan
Yüksek Lisans, Elektrik Elektronik Mühendisliği Bölümü
Tez Yöneticisi: Doç. Dr. Lale Alatan

Eylül 2016, 74 sayfa

Karakteristik modlar teorisi son yıllarda anten tasarımı için yaygın olarak kullanılmaktadır. Bu teori, iletken gövdelerin saçılım ve yayılım özelliklerine fiziksel bakış açısı getirmektedir. Bu tez çalışmasında, baskılı yapıların karakteristik mod teorisi kullanılarak analiz edilebilmesi için bir MATLAB kodu geliştirilmiştir. Baskılı yapıların karakteristik modları, yapıya bağlı olarak değişen momentler yöntemi (MoM) matrisi kullanılarak hesaplanabilmektedir. MoM matrisinin oluşturulabilmesi için, Rao Wilton Glisson (RWG) temel fonksiyonu ve Galerkin'in test prosedürü kullanılarak elektrik alan integral denklemi ayrıklaştırılmıştır. İlk olarak, geliştirilen kod kullanılarak çok geniş bantlı düzlemsel konik-şekilli sözde-monopol anten yapısının karakteristik mod analizi yapılmıştır. Sonuçlar, ticari elektromanyetik benzetim yazılımı FEKO'dan elde edilen sonuçlarla karşılaştırılmıştır. Bu karşılaştırma ile geliştirilen kodun isabetliliği doğrulandıktan sonra, kod dielektrik taban malzemesine basılı antenlerin analizini de yapabilecek şekilde genişletilmiştir. Bu amaçla, katmanlı ortamlarda uzamsal Green's fonksiyonlarını elde etmek için ayrık kompleks görüntü yönteminden yararlanılmıştır. Geliştirilen kod kullanılarak dikdörtgensel

mikroşerit antenlerin analizi gerçekleştirilmiş ve sonuçlar FEKO ile karşılaştırılmıştır.

Anahtar kelimeler: Karakteristik modlar, momentler metodu, nümerik analiz, baskılı antenler, giriş empedansı.

To my beloved wife

ACKNOWLEDGEMENTS

I would like to express my sincere thanks to my supervisor Assoc. Prof. Dr. Lale Alatan for her support and motivating guidance throughout this thesis study.

I also would like to thank to ASELSAN Inc. for resources and facilities that I used throughout this thesis.

I am grateful to Assist. Prof. Dr. Aytaç Alparslan, Assist. Prof. Dr. Emine Pınar Karabulut for providing me their MATLAB codes about DCIM and to Mehmet Nazım Batur for his support.

Besides, I would like to thank to Dr. Bülent Alıcıoğlu and Cengiz Çetinkaya for their support and motivation throughout this study.

I am also grateful to my dear friend Furkan Aral Tunç for his support, motivation and helps during my studies.

I owe special thanks to my parents for their infinite love, support, encouragement and sacrifices during my academic life.

Finally, I would like to express my sincere thanks to my dear wife, Mine Çelik Çetin. This thesis study would not be completed without her endless support, infinite patience and love.

TABLE OF CONTENTS

ABSTRACT v

ÖZ vii

ACKNOWLEDGEMENTS x

TABLE OF CONTENTS xi

LIST OF TABLES xv

LIST OF ABBREVATIONS xvi

CHAPTERS

1. INTRODUCTION 1

2. THE THEORY OF CHARACTERISTIC MODES 7

2.1. MoM Solution of EFIE Using RWG Basis Function 12
2.1.1. EFIE Formulation 12
2.1.2. RWG Basis Function 13
2.1.3. Method of Moments Formulation with Galerkin's Testing 15
2.2. Green's Functions for Layered Media 19
2.3. Feed Model for Microstrip Antennas and Input Impedance Calculation 21
2.4. Development of the Code 24

3. NUMERICAL RESULTS 29

3.1. Analysis of Rectangular Patch 29
3.1.1. Scattering Analysis 30
3.1.2. Characteristic Mode Analysis 32
3.2. Characteristic Mode Analysis of the Bevel-Shaped Antenna 39
3.3. Analysis of Rectangular Microstrip Patch Antenna 48
3.3.1. Observation of the Characteristic Modes 49

3.3.2. Computation of the Input Admittance 57
4. CONCLUSION AND FUTURE WORK 65
4.1. Future Studies 66
REFERENCES 69

LIST OF FIGURES

FIGURES

Figure 1 The fundamental structure of RWG basis function [34] 14
Figure 2 Barycentric subdivision of an RWG edge element 19
Figure 3 Current amplitude on the RWG basis function 22
Figure 4 Current amplitude on the modified RWG basis function 22
Figure 5 Triangulated square patch example 26
Figure 6 Triangle pairs of triangulated square patch example 26
Figure 7 Current distribution for x-polarized incident electric field 30
Figure 8 Current distribution for y-polarized incident electric field 31
Figure 9 Current distribution for xy-polarized incident electric field 31
Figure 10 Current distributions presented in [5] 33
Figure 11 Current distribution for J_0 33
Figure 12 Current distribution for J_1 34
Figure 13 Current distribution for J_2 34
Figure 14 Current distribution for J_3 35
Figure 15 Current distribution for J_4 35
Figure 16 Current distribution for J_5 36
Figure 17 Bevel-shaped antenna geometry 39
Figure 18 Meshed structure in FEKO 40
Figure 19 Meshed structure in GMSH 40
Figure 20 Eigenvalues of the 1st interested mode 42
Figure 21 MS values of the 1st interested mode 42
Figure 22 Eigenvalues of the 2nd interested mode 43
Figure 23 MS values of the 2nd interested mode 43

Figure 24 Eigenvalues of the 3rd interested mode.....44
Figure 25 MS values of the 3rd interested mode 44
Figure 26 Current distribution of the 1st interested mode obtained from FEKO ...45
Figure 27 Current distribution of the 2nd interested mode obtained from FEKO ..45
Figure 28 Current distribution of the 3rd interested mode obtained from FEKO...46
Figure 29 Current distribution of the 1st interested mode obtained from code.....47
Figure 30 Current distribution of the 2nd interested mode obtained from code.....47
Figure 31 Current distribution of the 3rd interested mode obtained from code.....48
Figure 32 2D meshed antenna structure without feeding in PDE Toolbox 50
Figure 33 2D meshed antenna structure without feeding in FEKO.....50
Figure 34 Eigenvalues of the 1st mode of antenna structure.....51
Figure 35 MS values of the 1st mode of antenna structure 51
Figure 36 Current distribution of the 1st mode obtained by code 52
Figure 37 Current distribution of the 1st mode obtained by FEKO 53
Figure 38 Eigenvalues of the 2nd mode of antenna structure.....54
Figure 39 MS values of the 2nd mode of antenna structure.....54
Figure 40 Current distribution of the 2nd mode obtained by code 55
Figure 41 Current distribution of the 2nd mode obtained by FEKO 56
Figure 42 3D coaxial probe fed microstrip antenna model in FEKO 57
Figure 43 Real part of input admittance for the feed position (-6, 0) 58
Figure 44 Imaginary part of input admittance for the feed position (-6, 0) 59
Figure 45 Magnitude of input admittance for the feed position (-6, 0) 59
Figure 46 Real part of input admittance for the feed position (0, -6) 60
Figure 47 Imaginary part of input admittance for the feed position (0, -6) 60
Figure 48 Magnitude of input admittance for the feed position (0, -6) 61

LIST OF TABLES

TABLES

Table 1 Current schematics of the modes.....37
Table 2 Modal excitation coefficients of the modes.....38
Table 3 Modal significances and modal excitation coefficients of the modes 62

LIST OF ABBREVATIONS

MoM: Method of Moments

RWG: Rao Wilton Glisson

EFIE: Electric Field Integral Equation

DCIM: Discrete Complex Image Method

MS: Modal Significance

CHAPTER 1

INTRODUCTION

Antenna design for RF systems has been one of the main problems for microwave engineers for decades. In recent years, developments in RF based systems such as wireless communication systems, radars and navigation systems have been increased significantly. Therefore, antenna design has become a more important issue.

An analytical analysis method does not exist for complicated printed antenna geometries. Therefore, numerical methods and commercial electromagnetic field simulators such as HFSS [1], FEKO [2] or CST [3] becomes necessary for antenna design [4]. However, the performances of the antennas which have been designed by using design methods supported by electromagnetic simulators rely on the designer's experience. Moreover, when these methods are used, the physical insight for radiating behavior is usually overlooked. Integration of the theory of characteristic modes into the antenna design process can deal with this problem and effective usage of characteristic modes provides designer a controlled design strategy for antenna design [5].

The theory of characteristic modes was first put forward by Garbacz in 1968 [6]. Garbacz defined the characteristic modes and stated that every conducting obstacle has a particular set of surface currents at each frequency. Garbacz and Turpin suggested that these surface currents and related electric fields do not depend on any excitation; these are the characteristics that depend on the shape of the conducting obstacle [7]. It is also shown that the scattering behavior of the

obstacle can be obtained if characteristic modes of the obstacle are known; thus scattered fields at the far zone can be found by using the characteristic modes as a basis set. Computational techniques to find characteristic modes of thin wire scatterers are developed [7, 8, 9] and these techniques are applied to compute characteristic mode current distributions of straight wires, circular loops, elliptical loops, circular arcs and helices. In 1971, Harrington and Mautz generalized the theory of characteristic modes to the analysis of 3D conducting bodies by utilizing Method of Moments (MoM) [10] formulation [11]. They explained that characteristic currents form a weighted orthogonal set over the surface of conducting bodies, and the fields due to these characteristic currents form an orthogonal set over a sphere at infinity. In MoM, the unknown induced currents on the conducting body are expanded in terms of known basis functions and a matrix equation is obtained to solve the unknown coefficients of these basis functions by using the vanishing tangential electric field boundary condition on the surface of the conducting body. By diagonalizing this matrix, formulas to compute the characteristic currents are developed. Moreover, Harrington and Mautz also developed a straightforward computation procedure to find characteristic modes [12]. Since a method to efficiently compute the characteristic modes became available, the theory of characteristic modes has become more useful for antenna design. In 1982, Garbacz and Pozar focused on directly to the antenna shape synthesis problem. For example, instead of reactive load synthesis in a given conducting body to obtain a desired scattering pattern, the synthesis of the conducting body's shape is proposed [13]. Although the theory of characteristic modes were studied extensively in the 70s, the theory fell into disuse in the 80s; because computation requirements for the extraction of characteristic modes of more complicated antenna structures exceeded the capacity of available computational power [5]. In recent years, computers and computation tools have been improved and the theory of characteristic modes has become more popular, especially for antenna design problems.

The theory of characteristic modes are interesting for antenna design because these modes provide physical insight about radiating behavior of the antenna [4]. A good starting point for the optimization of antenna parameters can be provided by the theory of characteristic modes and consequently the number of iterations in the optimization cycle can be significantly reduced by using the theory of characteristic modes. Characteristic modes have also orthogonality properties and a few modes are sufficient to understand scattering phenomena of the conducting surface for electrically small sizes [11]. These properties make the characteristic modes more useful for antenna design work. The independency of characteristic modes from any excitation [4, 7] and dependency of them only on the shape and the size of conducting surface makes it possible to optimize the shape and size of the radiating surface of the antenna [4]. Selecting the feeding configuration for intended modes to be excited is also possible by using this property. The shape and size optimization and optimum feeding configuration selection are two vital steps of antenna design. These important steps can be clearly done by using the theory of characteristic modes.

In the last decade, the theory of characteristic modes is utilized in the analysis and design of antennas used for a wide variety of applications. For instance, in recent years multiple-input multiple-output (MIMO) antennas are designed by using the theory of characteristic modes. MIMO antennas are widely used in communication systems to increase the channel capacity [14]. Properties of characteristic modes such as orthogonality makes the theory useful for MIMO applications. Ethier, McNamara and Lanoue developed their MIMO antenna design approach based on the theory of characteristic modes. In particular, they used the theory to provide low correlation between antennas and higher gain values which are important specifications of MIMO antennas [15, 16]. Isolation between multiple ports is another important specification of MIMO antennas and it must be as high as possible. In [17], high isolation between multiple ports is achieved by taking into account the effects of characteristic current densities on the chassis of the antenna system. Li, Miers and Lau also used the theory of

characteristic modes on the chassis structure of orthogonal MIMO handset antennas. They managed to design efficient MIMO antennas with low correlation and low coupling by exciting the orthogonal characteristic modes [18]. Bandwidth enhancement is another important aim in MIMO antenna design. Miers, Li and Lau focused on this specification for multiband MIMO antenna design by using the theory of characteristic modes [19]. Deng, Feng and Hum also concentrated on the same specification by considering characteristic mode analysis of the chassis of the MIMO mobile handset antenna [20]. Another bandwidth concerned MIMO antenna design by using the theory of characteristic modes is made by Manteuffel and Martens. They designed compact multimode multielement antenna for the application of ultra wideband massive MIMO indoor base stations which provide ultra-high data rate [21]. To obtain requirements of MIMO antennas mentioned above, characteristic mode theory is used for systematic shape optimization of symmetric MIMO antennas [14]. In MIMO applications, the theory of characteristic modes is also used for pattern diversity [22].

Another important application of the theory of characteristic modes is platform-mounted antenna design in high frequency (HF) band. In this design concept, the platform is assumed as the main radiator and the HF antennas mounted on the platform behaves as the coupling mechanism [23]. For example, Chen and Wang designed an HF antenna for unmanned aerial vehicle (UAV) by utilizing the theory of characteristic modes on the UAV body [24]. They also applied the same design concept to the shipboard-mounted HF band antenna design by analyzing the characteristic modes of the shipboard [25]. Like MIMO antennas, enhancement of bandwidth is a significant problem for HF antennas. Shih and Behdad handled this problem by using the theory of characteristic modes for platform-mounted HF antennas [23].

Design methods based on the theory of characteristic modes is also used in the design of reactively loaded dipole antennas. For example, Obeidat, Raines and Rojas used the theory of network characteristic modes in the design of broadband

antennas to optimize the load values and positions [26]. They also used this technique to compute reactive load values in frequency reconfigurable antenna design [27]. Characteristic modes theory is also employed with differential evolution algorithm in synthesis of reactively controlled antenna arrays [28].

In recent years, the theory of characteristic modes is utilized in order to design compact and miniaturized antennas for devices which have limited space for antennas, such as smart phones. Martens and Manteuffel designed a three-port MIMO antenna system for small terminals, which can be used in smart phones [29]. The theory of characteristic modes is also used to design wireless universal serial bus (USB) dongle antenna for wireless local area network (WLAN) applications [30] and to design a compact metallic strip antenna which is manufactured with low temperature co-fired ceramic (LTCC) technology [31]. Finally, to facilitate the efficient MoM analysis of large scale reflectarrays, the use of characteristic modes as macro basis functions is proposed in [32].

In this thesis, a code is developed to analyze characteristic modes of printed structures. The code is developed in MATLAB [33] environment. MoM with Rao Wilton Glisson (RWG) basis function [34] and Galerkin testing method [10] is used. The Electric Field Integral Equation (EFIE) [34] is used in order to obtain the MoM matrix which is called impedance matrix. The developed code is first tested by choosing rectangular conducting patch as a basic geometry whose scattering behavior is easy to understand. In order to mesh the rectangular patch, MATLAB Partial Differential Equation (PDE) Toolbox [35] is used. Incident fields with different polarizations are applied to rectangular conducting patch to test the code. The characteristic mode currents, related parameters such as eigenvalues and associated eigencurrents are computed. Then the developed code is applied to analyze characteristic modes of an ultra wide band printed planar bevel-shaped quasi-monopole antenna. The mesh generator program called GMSH [36] is used to mesh this antenna structure.

This thesis also includes the characteristic mode analysis of a rectangular microstrip patch antenna as a printed structure. The MoM analysis of printed structures requires the computation of the spatial domain Green's functions in layered media. For this purpose, the discrete complex image method (DCIM) [37] is used on the codes developed by Aksun and his group [38-40] are utilized.

This thesis is outlined as follows: In Chapter 2, the theory of characteristic modes is briefly discussed. Theoretical information about RWG basis function and MoM solution of the electric field integral equation which are fundamental parts of the developed code are given. While finding the impedance matrix, a function developed by Makarov [41] is modified and used, modification details are presented in this chapter. Development steps of the code and important details about algorithms are also explained in this chapter.

Chapter 3 starts with the application of the developed code to the analysis of rectangular conducting patch. Then an ultra wide band planar bevel-shaped quasi-monopole antenna is studied. The results obtained by using the commercial electromagnetic simulator FEKO and by using the developed code in MATLAB environment are presented and compared. Finally, a rectangular microstrip patch antenna is considered. For this antenna, in addition to the characteristic modes, the input impedance of the antenna is also studied for different feed positions. The analysis results obtained by using the developed code are compared with FEKO analysis results.

Finally, the most important results obtained from this thesis are summarized and the information about future studies based on this work is given in Chapter 4.

CHAPTER 2

THE THEORY OF CHARACTERISTIC MODES

Fundamental principles of the theory of characteristic modes are discussed in this chapter. The characteristic modes can be computed numerically by utilizing the impedance matrix constructed during the MoM solution of the structure. The MoM solution of printed structures in layered media is also discussed. Development steps of the code and important details about the utilized algorithms are explained. Note that $e^{j\omega t}$ time dependence is assumed and suppressed throughout this thesis.

Assume that there is a conducting body which is defined by the surface *S*. The conducting body is in an impressed electric field $\boldsymbol{E^i}$. An operator equation is defined for the current $\boldsymbol{J}$ on the surface *S*

$$[L(\boldsymbol{J}) - \boldsymbol{E^i}]_{tan} = 0 \tag{2.1}$$

where the subscript "*tan*" denotes the tangential components on *S*. The operator *L* is defined by [11]

$$L(\boldsymbol{J}) = j\omega \boldsymbol{A}(\boldsymbol{J}) + \boldsymbol{\nabla}\Phi(\boldsymbol{J}) \tag{2.2}$$

$$\boldsymbol{A}(\boldsymbol{J}) = \mu \oiint_S \boldsymbol{J}(\boldsymbol{r}')\psi(\boldsymbol{r},\boldsymbol{r}')ds' \tag{2.3}$$

$$\Phi(\boldsymbol{J}) = -\frac{1}{j\omega\epsilon} \oiint_S \nabla' \cdot \boldsymbol{J}(\boldsymbol{r}')\psi(\boldsymbol{r},\boldsymbol{r}')ds' \tag{2.4}$$

$$\psi(\boldsymbol{r},\boldsymbol{r}') = \frac{e^{-jk|\boldsymbol{r}-\boldsymbol{r}'|}}{4\pi|\boldsymbol{r}-\boldsymbol{r}'|} \tag{2.5}$$

where ϵ, μ and k are the permittivity, the permeability and the wave number, respectively, and ψ is the Green's function corresponding to the medium that the analyzed conducting body exists. $L(\boldsymbol{J})$ in (2.1) represents the electric field intensity ($\boldsymbol{E}$) caused by the current $\boldsymbol{J}$ on the surface S. Hence the L operator can be considered as an impedance operator and it can be conveniently replaced by operator Z in the following form to be consistent with literature.

$$Z(\boldsymbol{J}) = [L(\boldsymbol{J})]_{tan} \tag{2.6}$$

Z is a linear operator for linear media. Moreover, Z is a symmetric operator due to reciprocity theorem [42]. Therefore, the real and imaginary parts of Z, R and X, respectively, are real symmetric operators and defined by

$$R(\boldsymbol{J}) = \frac{1}{2}(Z(\boldsymbol{J}) + Z^*(\boldsymbol{J})) \tag{2.7}$$

$$X(\boldsymbol{J}) = \frac{1}{2j}(Z(\boldsymbol{J}) - Z^*(\boldsymbol{J})) \tag{2.8}$$

Note that, since the power radiated by current $\boldsymbol{J}$ on S is non-negative, the operator R is positive semidefinite.

Consider the following eigenvalue equation

$$Z(\boldsymbol{J_n}) = \nu_n R(\boldsymbol{J_n}) \tag{2.9}$$

$$(R + jX)(\boldsymbol{J_n}) = \nu_n R(\boldsymbol{J_n}) \tag{2.10}$$

where ν_n are eigenvalues, and $\boldsymbol{J_n}$ are eigenfunctions. The eigenfunctions $\boldsymbol{J_n}$ are named as the eigencurrents or characteristic currents of the conducting body defined by S.

By defining $\nu_n = 1 + j\lambda_n$, the eigenvalue equation becomes

$$X(\boldsymbol{J_n}) = \lambda_n R(\boldsymbol{J_n}) \tag{2.11}$$

Eigenvalues λ_n and eigenfunctions $\boldsymbol{J_n}$ must be real, since X and R are real symmetric operators. Moreover, the following orthogonality relationships are satisfied by the eigenfunctions $\boldsymbol{J_n}$.

$$\left.\begin{aligned} \langle \boldsymbol{J_m}, R\boldsymbol{J_n} \rangle &= 0 \quad (2.12) \\ \langle \boldsymbol{J_m}, X\boldsymbol{J_n} \rangle &= 0 \quad (2.13) \\ \langle \boldsymbol{J_m}, Z\boldsymbol{J_n} \rangle &= 0 \quad (2.14) \end{aligned}\right\} \text{for } m \neq n$$

The following orthogonality relationships must also be satisfied.

$$\left.\begin{aligned} \langle \boldsymbol{J_m^*}, R\boldsymbol{J_n} \rangle &= 0 \quad (2.15) \\ \langle \boldsymbol{J_m^*}, X\boldsymbol{J_n} \rangle &= 0 \quad (2.16) \\ \langle \boldsymbol{J_m^*}, Z\boldsymbol{J_n} \rangle &= 0 \quad (2.17) \end{aligned}\right\} \text{for } m \neq n$$

Eigencurrents can be normalized according to the radiated power as:

$$\langle \boldsymbol{J_n^*}, R\boldsymbol{J_n} \rangle = 1 \quad (2.18)$$

After normalization, the orthogonality relationships (2.12), (2.13), (2.14) and (2.15), (2.16), (2.17) can be combined and stated as:

$$\langle \boldsymbol{J_m}, R\boldsymbol{J_n} \rangle = \langle \boldsymbol{J_m^*}, R\boldsymbol{J_n} \rangle = \delta_{mn} \quad (2.19)$$

$$\langle \boldsymbol{J_m}, X\boldsymbol{J_n} \rangle = \langle \boldsymbol{J_m^*}, X\boldsymbol{J_n} \rangle = \lambda_n \delta_{mn} \quad (2.20)$$

$$\langle \boldsymbol{J_m}, Z\boldsymbol{J_n} \rangle = \langle \boldsymbol{J_m^*}, Z\boldsymbol{J_n} \rangle = (1 + j\lambda_n)\delta_{mn} \quad (2.21)$$

where δ_{mn} is the Kronecker delta (0 if $m \neq n$, and 1 if $m = n$). Throughout this thesis $\boldsymbol{J_n}$ refers to normalized eigencurrents.

Recall the complex Poynting theorem [42]:

$$\langle \boldsymbol{J}^*, Z\boldsymbol{J} \rangle = \langle \boldsymbol{J}^*, R\boldsymbol{J} \rangle + j\langle \boldsymbol{J}^*, XJ \rangle$$

$$= \oiint_{S'} \boldsymbol{E} \times \boldsymbol{H}^* \cdot ds + j\omega \iiint_{V'} (\mu \boldsymbol{H} \cdot \boldsymbol{H}^* - \epsilon \boldsymbol{E} \cdot \boldsymbol{E}^*) dv \qquad (2.22)$$

where S' is a surface enclosing S and V' is the volume enclosed by S'.

By using the orthogonality relations, the complex Poynting theorem can be expressed in terms of characteristic fields (or eigenfields), $\boldsymbol{E_n}$ and $\boldsymbol{H_n}$, as:

$$\oiint_{S'} \boldsymbol{E_m} \times \boldsymbol{H_n^*} \cdot ds + j\omega \iiint_{V'} (\mu \boldsymbol{H_m} \cdot \boldsymbol{H_n^*} - \epsilon \boldsymbol{E_m} \cdot \boldsymbol{E_n^*}) dv$$

$$= (1 + j\lambda_n)\delta_{mn} \qquad (2.23)$$

Important discussions about the eigenvalues λ_n can be deduced from equation (2.23). The eigenvalues give information about the resonance frequency and the radiating behavior of the corresponding characteristic modes [4]. Modes which have positive eigenvalues store magnetic energy and these modes are called inductive modes. On the other hand, modes which have negative eigenvalues store electric energy and these modes are called capacitive modes. Mode which has zero eigenvalue is called resonant mode. Hence information about the resonance frequency of the characteristic modes can be obtained by using eigenvalues.

Due to the orthogonality property of the eigencurrents, the total current on $\boldsymbol{J}$ can be expanded in terms of eigencurrents as:

$$\boldsymbol{J} = \sum_n \alpha_n \boldsymbol{J_n} \qquad (2.24)$$

where the α_n's are the coefficients of each mode. By substituting this expansion into (2.1), following relation is obtained:

$$[\sum_n \alpha_n L\boldsymbol{J_n} - \boldsymbol{E^i}]_{tan} = 0 \qquad (2.25)$$

By taking the inner product of (2.25) with each $\boldsymbol{J_m}$, and using (2.6), the following set of equations are obtained for $m = 1, 2, 3, \cdots$

$$\sum_n \alpha_n \langle \boldsymbol{J_m}, Z\boldsymbol{J_n} \rangle - \langle \boldsymbol{J_m}, \boldsymbol{E^i} \rangle = 0 \qquad (2.26)$$

Due to the orthogonality property of eigencurrents, (2.26) reduces to

$$\alpha_n(1 + j\lambda_n) = \langle \boldsymbol{J_n}, \boldsymbol{E^i} \rangle \tag{2.27}$$

The term which is on the right-hand side of (2.27) is called the modal excitation coefficient V_n^i

$$V_n^i = \langle \boldsymbol{J_n}, \boldsymbol{E^i} \rangle = \oiint_S \boldsymbol{J_n} \cdot \boldsymbol{E^i}\, ds \tag{2.28}$$

Substituting coefficients α_n obtained from (2.27) into (2.24), the modal solution for the total current $\boldsymbol{J}$ on S is acquired as:

$$\boldsymbol{J} = \sum_n \frac{V_n^i}{1+j\lambda_n} \boldsymbol{J_n} \tag{2.29}$$

Similarly the electric and magnetic fields can also be expanded in terms of eigenfields as:

$$\boldsymbol{E} = \sum_n \frac{V_n^i}{1+j\lambda_n} \boldsymbol{E_n} \tag{2.30}$$

$$\boldsymbol{H} = \sum_n \frac{V_n^i}{1+j\lambda_n} \boldsymbol{H_n} \tag{2.31}$$

It is obvious from (2.29) that eigenvalues which have smaller magnitudes are more dominant than the other modes.

As the modal solution of the total current $\boldsymbol{J}$ in (2.29) is inversely proportional with the term "$1 + j\lambda_n$", modal significance (MS) is defined as [5]:

$$MS_n = \left| \frac{1}{1+j\lambda_n} \right| \tag{2.32}$$

Modal significance denotes the normalized amplitude of the characteristic modes [43] and the mode which has a modal significance value closer to 1, is the dominant mode. Modal significance does not depend on any excitation, it depends on only the shape and size of the conducting body. On the other hand, modal excitation coefficient V_n^i is determined by the excitation. Hence there are two

factors that determine how strongly a mode will be excited; namely modal significance and modal excitation coefficient. A mode may be the dominant mode due to its modal significance value but it may not be excited at all due to its small modal excitation coefficient.

2.1. MoM Solution of EFIE Using RWG Basis Function

In this thesis, for the numerical computation of the characteristic currents of the conducting body, the MoM [10] is used and the *Z* operator is converted into a matrix as suggested in [12].

In this section, background information about EFIE and RWG basis functions used in MoM solution is presented briefly. Formulation of MoM solution of EFIE by using RWG basis functions is also explained from the code development perspective.

2.1.1. EFIE Formulation

The EFIE is an integral equation in terms of the surface current induced on a conducting body due to an impressed source. As the name implies it is obtained by using the boundary condition on the electric field [34].

Assume that there is an open or closed perfectly conducting body which is defined by the surface *S*. The conducting body is in an impressed electric field $\boldsymbol{E^i}$ which induces surface currents $\boldsymbol{J}$ on *S*. The scattered electric field $\boldsymbol{E^s}$ from the conducting body is calculated from the surface current by

$$\boldsymbol{E^s} = -j\omega\boldsymbol{A} - \nabla\Phi \tag{2.33}$$

with the magnetic vector potential $\boldsymbol{A}$ and the scalar potential Φ defined as:

$$\boldsymbol{A}(\boldsymbol{r}) = \frac{\mu}{4\pi}\int_S \frac{e^{-jk|\boldsymbol{r}-\boldsymbol{r}'|}}{|\boldsymbol{r}-\boldsymbol{r}'|}\boldsymbol{J}(\boldsymbol{r}')ds' \tag{2.34}$$

$$\Phi(\boldsymbol{r}) = \frac{1}{4\pi\epsilon}\int_S \frac{e^{-jk|\boldsymbol{r}-\boldsymbol{r}'|}}{|\boldsymbol{r}-\boldsymbol{r}'|}\rho ds' \tag{2.35}$$

where ρ is the surface charge density, ϵ, μ and k are the permittivity, the permeability and the wave number, respectively, of the surrounding homogeneous medium. $\boldsymbol{J}$ and ρ are related to each other through the continuity equation:

$$\boldsymbol{\nabla_S} \cdot \boldsymbol{J} = -j\omega\rho \tag{2.36}$$

An integrodifferential equation for current $\boldsymbol{J}$ is obtained by utilizing the boundary condition $\hat{\boldsymbol{n}} \times (\boldsymbol{E^i} + \boldsymbol{E^s}) = 0$ on S

$$-\boldsymbol{E^i_{tan}} = (-j\omega\frac{\mu}{4\pi}\int_S \frac{e^{-jk|\boldsymbol{r}-\boldsymbol{r}'|}}{|\boldsymbol{r}-\boldsymbol{r}'|}\boldsymbol{J}(\boldsymbol{r}')ds' - \boldsymbol{\nabla}\frac{1}{4\pi\epsilon}\int_S \frac{e^{-jk|\boldsymbol{r}-\boldsymbol{r}'|}}{|\boldsymbol{r}-\boldsymbol{r}'|}\rho ds')_{tan} \tag{2.37}$$

The EFIE formulation is preferred in this thesis since it is more appropriate for modeling radiating structures like antennas because it is applicable to both open and closed conducting surfaces, whereas magnetic field integral equation (MFIE) is applicable only to closed conducting surfaces.

2.1.2. RWG Basis Function

The structural and numerical information about RWG basis function is given in this part. Planar triangular surface patch model is suitable for modeling arbitrarily shaped conducting surfaces due to three important properties. Planar triangular patch model can be adapted to different surface geometries, triangular patches can be defined easily for computer input and density of triangular patches can be determined according to the required resolution in the conducting surface [34]. RWG basis function is used in triangular patch modeling approach. It is a subdomain-type basis function that is defined on pairs of adjacent triangular patches. At subdomain boundaries, RWG basis function provides a current representation free of line or point charges.

Assume that the conducting surface *S* is triangulated properly and this triangulation is described in terms of convenient set of faces, edges, vertices and boundary edges. Each basis function on the surface *S* is related to an interior edge, such as nonboundary edges, which connects two triangles. In other words, each basis function has two triangles sharing the common edge [41]. The fundamental structure of the RWG basis function is illustrated in the Figure 1.

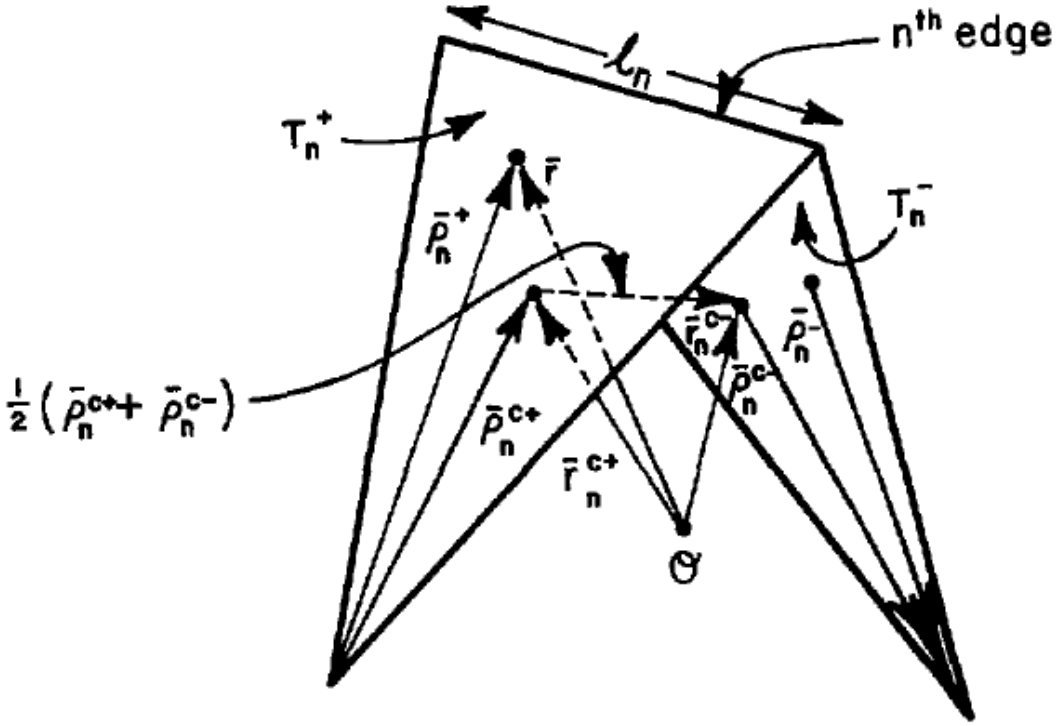

Figure 1 The fundamental structure of RWG basis function [34]

As seen in Figure 2, there are two triangles, T_n^+ and T_n^-, connected with each other by the n^{th} edge of a triangulated conducting surface. Positive and negative current reference directions are symbolized by the plus and minus signs, respectively. Current towards n^{th} edge refers to positive current and current from n^{th} edge refers to negative current. Points in triangle T_n^+ can be specified by the position vector $\boldsymbol{\rho_n^+}$ defined from the free vertex of the triangle T_n^+. Points in triangle T_n^- can be specified similarly; but instead of the position vector $\boldsymbol{\rho_n^+}$, the position vector $\boldsymbol{\rho_n^-}$ defined toward to the free vertex of the triangle T_n^- is used. RWG basis function associated with the n^{th} edge is described as:

$$f_n(r) = \begin{cases} (l_n/2A_n^+)\,\boldsymbol{\rho_n^+}, & \boldsymbol{r}\ in\ T_n^+ \\ (l_n/2A_n^-)\,\boldsymbol{\rho_n^-}, & \boldsymbol{r}\ in\ T_n^- \\ 0, & otherwise \end{cases} \tag{2.38}$$

where l_n is the edge length of n^{th} edge, $A_n^{\pm}$ is the area of the triangle $T_n^{\pm}$ and $\boldsymbol{r}$ is the position vector defined from origin (O). Note that the normal component of the currents at the outer boundary edges of RWG triangle pair are zero and the normal component of the current at the n^{th} edge is constant along the edge and it is continuous across the edge.

As the surface divergence in $T_n^{\pm}$ is $(\pm 1/\boldsymbol{\rho_n^{\pm}})\,\partial(\boldsymbol{\rho_n^{\pm}} f_n)/\partial \boldsymbol{\rho_n^{\pm}}$; the surface divergence of the basis function f_n, which is proportional to the surface charge density can be expressed as:

$$\nabla_s \cdot f_n = \begin{cases} (l_n/A_n^+), & \boldsymbol{r}\ in\ T_n^+ \\ -(l_n/A_n^-), & \boldsymbol{r}\ in\ T_n^- \\ 0, & otherwise \end{cases} \tag{2.39}$$

From equation (2.39), it can be seen that the charge density is constant over each triangle and the total charge related to the triangle pair T_n^+ and T_n^- is zero.

2.1.3. Method of Moments Formulation with Galerkin's Testing

The MoM will be applied to solve the unknown current density in the EFIE given in (2.37). As the first step of the MoM procedure, unknown current density $\boldsymbol{J}$ is expanded in terms of RWG basis functions as:

$$\boldsymbol{J} \cong \sum_{n=1}^{N} I_n f_n(r) \tag{2.40}$$

where N is the number of interior edges and I_n's are the unknown coefficients to be determined [34].

Substitute (2.40) into (2.37) and define the following parameters for the sake of brevity

$$\boldsymbol{A_n}(\boldsymbol{r}) = \frac{\mu}{4\pi}\int_{T_n^+ + T_n^-} \frac{e^{-jk|\boldsymbol{r}-\boldsymbol{r}'|}}{|\boldsymbol{r}-\boldsymbol{r}'|} f_n ds' \tag{2.41}$$

$$\Phi_n(\boldsymbol{r}) = \frac{1}{4\pi\epsilon}\int_{T_n^+ + T_n^-} \frac{e^{-jk|\boldsymbol{r}-\boldsymbol{r}'|}}{|\boldsymbol{r}-\boldsymbol{r}'|} \frac{\nabla_s \cdot f_n}{-j\omega} ds' \tag{2.42}$$

Then (2.37) takes the following approximate form

$$\boldsymbol{E^i}(\boldsymbol{r}) \cong j\omega \boldsymbol{A_n}(\boldsymbol{r}) + \boldsymbol{\nabla}\Phi_n(\boldsymbol{r}) \tag{2.43}$$

As the next step of the MoM procedure (2.43) needs to be tested by a proper choice of testing functions. Galerkin's procedure is preferred, therefore testing functions are chosen to be same as basis functions (RWGs). After applying the testing, the following set of equations are obtained for $m = 1, 2, 3, \cdots, N$

$$\langle f_m, \boldsymbol{E^i}\rangle = j\omega\langle f_m, \boldsymbol{A_n}\rangle + \langle f_m, \boldsymbol{\nabla}\Phi_n\rangle \tag{2.44}$$

By using the properties of RWG functions and surface vector calculus, the last term in (2.44) can be converted into the following form:

$$\langle f_m, \boldsymbol{\nabla}\Phi_n\rangle = -\int_{T_m^+ + T_m^-} \Phi_n \nabla_s \cdot f_m \, ds \tag{2.45}$$

By using (2.39), and approximating the surface integral with the product of the potential at the centroid of the triangle and the area of the triangle, (2.45) simplifies to the following form:

$$\int_{T_m^+ + T_m^-} \Phi_n \nabla_s \cdot f_m \, ds$$

$$= l_m \left(\frac{1}{A_m^+}\int_{T_m^+} \Phi_n \, ds - \frac{1}{A_m^-}\int_{T_m^-} \Phi_n \, ds \right) \cong l_m[\Phi_n(\boldsymbol{r_m^{c+}}) - \Phi_n(\boldsymbol{r_m^{c-}})] \tag{2.46}$$

where $\boldsymbol{r_m^{c\pm}}$ is the position vector $\boldsymbol{r}$ at the centroid of $T_m^{\pm}$ triangle.

Note that the average of Φ over the triangle is approximated by the value of Φ at the centroid of the triangle. Using similar approximation for the integrals over the incident field and the vector potential, the following equations can be obtained:

$$\left\langle f_m, \begin{Bmatrix} \boldsymbol{E^i} \\ \boldsymbol{A_n} \end{Bmatrix} \right\rangle = l_m \left[\frac{1}{2A_m^+} \int_{T_m^+} \begin{Bmatrix} \boldsymbol{E^i} \\ \boldsymbol{A_n} \end{Bmatrix} \cdot \boldsymbol{\rho_m^+}\, ds + \frac{1}{2A_m^-} \int_{T_m^-} \begin{Bmatrix} \boldsymbol{E^i} \\ \boldsymbol{A_n} \end{Bmatrix} \cdot \boldsymbol{\rho_m^-}\, ds \right]$$

$$\cong \frac{l_m}{2} \left[\begin{Bmatrix} \boldsymbol{E^i}(\boldsymbol{r_m^{c+}}) \\ \boldsymbol{A_n}(\boldsymbol{r_m^{c+}}) \end{Bmatrix} \cdot \boldsymbol{\rho_m^{c+}} + \begin{Bmatrix} \boldsymbol{E^i}(\boldsymbol{r_m^{c-}}) \\ \boldsymbol{A_n}(\boldsymbol{r_m^{c-}}) \end{Bmatrix} \cdot \boldsymbol{\rho_m^{c-}} \right] \tag{2.47}$$

By using equations (2.46) and (2.47), equation (2.44) can be approximated as:

$$j\omega l_m \left[\boldsymbol{A_n}(\boldsymbol{r_m^{c+}}) \cdot \frac{\boldsymbol{\rho_m^{c+}}}{2} + \boldsymbol{A_n}(\boldsymbol{r_m^{c-}}) \cdot \frac{\boldsymbol{\rho_m^{c-}}}{2} \right] + l_m [\Phi_n(\boldsymbol{r_m^{c-}}) - \Phi_n(\boldsymbol{r_m^{c+}})]$$

$$= l_m \left[\boldsymbol{E^i}(\boldsymbol{r_m^{c+}}) \cdot \frac{\boldsymbol{\rho_m^{c+}}}{2} + \boldsymbol{E^i}(\boldsymbol{r_m^{c-}}) \cdot \frac{\boldsymbol{\rho_m^{c-}}}{2} \right] \tag{2.48}$$

for $m = 1,2,3, \cdots, N$.

N number of equations in (2.48) can be written in the following matrix form:

$$ZI = V \tag{2.49}$$

where $Z = [Z_{mn}]$ is an $N \times N$ matrix and $I = [I_n]$ and $V = [V_n]$ are column vectors of length *N*. Elements of the equation (2.49), *Z* and *V* are expressed as:

$$Z_{mn} = j\omega \langle f_m, \boldsymbol{A_n} \rangle + \langle f_m, \boldsymbol{\nabla} \Phi_n \rangle$$

$$= l_m \left[j\omega \left(\boldsymbol{A_{mn}^+} \cdot \frac{\boldsymbol{\rho_m^{c+}}}{2} + \boldsymbol{A_{mn}^-} \cdot \frac{\boldsymbol{\rho_m^{c-}}}{2} \right) + \Phi_{mn}^- - \Phi_{mn}^+ \right] \tag{2.50}$$

$$V_m = \langle f_m, \boldsymbol{E^i} \rangle = l_m \left(\boldsymbol{E_m^+} \cdot \frac{\boldsymbol{\rho_m^{c+}}}{2} + \boldsymbol{E_m^-} \cdot \frac{\boldsymbol{\rho_m^{c-}}}{2} \right) \tag{2.51}$$

where

$$\boldsymbol{A_{mn}^{\pm}} = \frac{\mu}{4\pi} \int_{T_n^+ + T_n^-} f_n(r') \left(\frac{e^{-jk\boldsymbol{R_m^{\pm}}}}{\boldsymbol{R_m^{\pm}}} \right) ds' \tag{2.52}$$

$$\Phi_{mn}^{\pm} = -\frac{1}{4\pi j\omega\epsilon} \int_{T_n^+ + T_n^-} \nabla_S' \cdot f_n(r') \left(\frac{e^{-jk\boldsymbol{R_m^{\pm}}}}{\boldsymbol{R_m^{\pm}}} \right) ds' \tag{2.53}$$

where $\boldsymbol{R_m^{\pm}} = |\boldsymbol{r_m^{c\pm}} - \boldsymbol{r'}|$ and $\boldsymbol{E_m^{\pm}} = \boldsymbol{E^i}(\boldsymbol{r_m^{c\pm}})$. The incident plane wave can be described:

$$\boldsymbol{E^i}(\boldsymbol{r}) = \boldsymbol{E_0} e^{j\boldsymbol{k}\cdot\boldsymbol{r}} \tag{2.54}$$

where the propagation vector $\boldsymbol{k}$ is defined in terms of the angle of arrival of the plane wave (θ_0, ϕ_0) as:

$$\boldsymbol{k} = k(sin\,\theta_0\,cos\,\phi_0\,\hat{\boldsymbol{x}} + sin\,\theta_0\,sin\,\phi_0\,\hat{\boldsymbol{y}} + cos\,\theta_0\,\hat{\boldsymbol{z}}) \tag{2.55}$$

In order to solve the unknown current coefficient vector *I*, the elements of the MoM matrix *Z* and the vector *V* should be computed. The evaluation of the vector *V* is straightforward for plane wave excitation, however the evaluation of *Z* matrix entries requires the computation of surface integrals given in (2.52) and (2.53). As it is well known, a singularity problem occurs when the source and observation points coincide. Hence if the vector and scalar potential integrals given in (2.52) and (2.53), respectively, are also approximated by the average values at the centroids, the diagonal entries of MoM matrix will be infinite due to the overlapping basis and testing functions. However, if the vector and scalar potential integrals are evaluated numerically by choosing different quadrature points rather than the centroids, the singularity problem can be avoided as suggested in [41]. For the numerical integration of the potential integrals, barycentric subdivision method proposed in [44] is utilized. In this method, each triangle (primary triangle) is divided into 9 subtriangles (secondary triangles) by dividing each edge of the primary triangle into 3 equal segments. The barycentric subdivision for two adjacent primary triangles is illustrated in Figure 2.

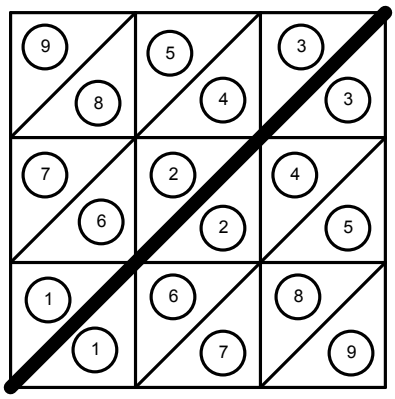

Figure 2 Barycentric subdivision of an RWG edge element

Then the potential integrals over each secondary triangle are approximated by the product of the integrand value at the centroid of the secondary triangle and the area of the secondary triangle. Finally, the integral approximations from 9 secondary triangles are summed up to find the corresponding result for the primary triangle. Since the centroids of primary and secondary triangles do not coincide, singularity is avoided.

2.2. Green's Functions for Layered Media

The formulation presented so far is applicable for the analysis of conducting bodies in homogeneous medium, hence free-space Green's function $\left(\frac{e^{-jk|\boldsymbol{r}-\boldsymbol{r}\prime|}}{4\pi|\boldsymbol{r}-\boldsymbol{r}\prime|}\right)$ is used in the computation of the vector and the scalar potentials. However, the scope of this thesis is the characteristic mode analysis of printed structures and printed structures generally reside in a three layered (air - dielectric substrate - ground plane) medium. Therefore, the free-space Green's function needs to be replaced with the Green's function corresponding to the layered medium. Unfortunately, the spatial domain Green's function for layered media can not be obtained in closed-form, it needs to be computed numerically from its spectral domain counterpart. DCIM is proposed in literature [37] to approximately express

the spatial domain Green's function in closed-form. The accuracy and efficiency of DCIM method is improved by Aksun and his group [38-40].

In DCIM method the spatial domain Green's functions for layered media is approximated as a summation of spherical waves emerging from complex distances with complex coefficients. These complex distances and coefficients are different for the vector and scalar potentials. They depend on the dielectric constant and thickness of the substrate and the frequency. Complex distances for the vector and scalar potentials can be expressed respectively as:

$$R_i^A = \sqrt{x^2 + y^2 + (-j\alpha_i^A)^2} \tag{2.56}$$

$$R_i^{\emptyset} = \sqrt{x^2 + y^2 + (-j\alpha_i^{\emptyset})^2} \tag{2.57}$$

where α_i^A and $\alpha_i^{\emptyset}$ are coefficients that are used to compute complex distances.

The corresponding spatial domain Green's functions for layered media can be expressed for the vector and scalar potentials respectively as:

$$\sum_{i=1}^{N} C_i^A \frac{e^{-jkR_i^A}}{4\pi R_i^A} \tag{2.58}$$

$$\sum_{i=1}^{N} C_i^{\emptyset} \frac{e^{-jkR_i^{\emptyset}}}{4\pi R_i^{\emptyset}} \tag{2.59}$$

where C_i^A and $C_i^{\emptyset}$ are complex coefficients of the spatial domain Green's functions for layered media.

In this thesis, to compute these distances and coefficients, the code developed by Aytaç Alparslan [39] is utilized. Once the distances and coefficient values are available, the integrals in (2.52) and (2.53) can be computed as discussed in the previous section.

2.3. Feed Model for Microstrip Antennas and Input Impedance Calculation

To complete modal analysis of antennas, computation of the modal impedances for each mode and determination of the input impedance of the antenna are necessary. The modal impedances give information about which mode is most effective on the antenna behavior at specific frequency range [45]. Furthermore, the input impedance is utmost important parameter to find the optimum feed location.

It is possible to compute the input impedance of the antenna structure, Z_{in}, by using the modal parameters. This computation requires the construction of the excitation vector, V in the MoM matrix equation. Because modal excitation coefficients V_n^i's are found from the dot product of V and eigencurrent vector for n^{th} mode. To evaluate the V vector, the feeding structure and approach to model this feed should be chosen. Coaxial probe feed is considered and the current injected by the probe is modeled with a discontinuous RWG function. The discontinuity is assumed at the edge closest to the feed location. This discontinuous RWG element can be named as the source RWG.

In order to obtain discontinuity on current distribution, a minus sign is added to RWG basis function for minus triangle. Since it is difficult the visualize the current distribution in two dimensions, a one dimensional variation along the line that connects the outer corners of an RWG element will be presented. For a regular RWG basis function, the change in current amplitude along this line is illustrated in Figure 3.

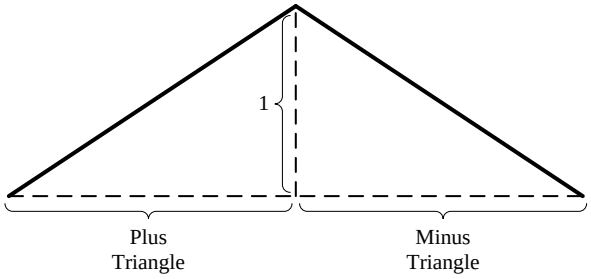

Figure 3 Current amplitude on the RWG basis function

The intended change in current amplitude for source RWG is illustrated in Figure 4.

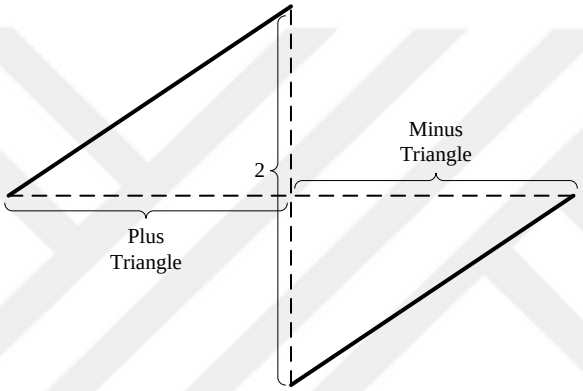

Figure 4 Current amplitude on the modified RWG basis function

The source RWG is expressed as:

$$f_{n,feed}(\boldsymbol{r}) = \begin{cases} (l_n/2A_n^+)\,\boldsymbol{\rho_n^+}, & \boldsymbol{r}\ in\ T_n^+ \\ -(l_n/2A_n^-)\,\boldsymbol{\rho_n^-}, & \boldsymbol{r}\ in\ T_n^- \\ 0, & otherwise \end{cases} \tag{2.60}$$

Note that, the product of the discontinuity in current density and the length of the corresponding edge will give the total current impressed by the probe ($I_{in} = 2l_n$).

The surface divergence of the basis function $f_{n,feed}$, is expressed as:

$$\nabla_s \cdot f_{n,feed}(\boldsymbol{r}) = \begin{cases} (l_n/A_n^+), & \boldsymbol{r}\ in\ T_n^+ \\ (l_n/A_n^-), & \boldsymbol{r}\ in\ T_n^- \\ 0, & otherwise \end{cases} \tag{2.61}$$

The expression for the entries of excitation vector *V* was derived in (2.51) as:

$$V_m = \langle f_m, \boldsymbol{E^i} \rangle = l_m \left(\boldsymbol{E_m^+} \cdot \frac{\boldsymbol{\rho_m^{c+}}}{2} + \boldsymbol{E_m^-} \cdot \frac{\boldsymbol{\rho_m^{c-}}}{2} \right)$$

where $\boldsymbol{E_m^{\pm}}$ is the incident electric field at the centroid of the $\pm$ triangle. To calculate the incident electric field, the vector and scalar potential integrals given in (2.52) and (2.53), respectively, are evaluated by replacing f_n's with source RWG.

Computation of the input impedance for the patch antenna is based on the formulation presented in the classical paper by Pozar [46]. Pozar used the following input impedance relation based on the power delivered by the source:

$$Z_{in} = \frac{P}{I_{in}^2} = -\int_V \frac{\boldsymbol{E} \cdot \boldsymbol{J_i} dv}{(I_{in})^2} \tag{2.62}$$

where $\boldsymbol{E}$ is the total electric field caused by the source current $\boldsymbol{J_i}$ and I_{in} is the current injected by the source. The power delivered by the source can also be written in terms of V and I vectors of MoM matrix equation by using reciprocity. Hence, the input impedance can be written as:

$$Z_{in} = -\frac{V^T I}{I_{in}^2} \tag{2.63}$$

In order to express input impedance in terms of modal parameters, replace I with its characteristic mode expansion. Then Z_{in} becomes:

$$Z_{in} = -\frac{V^T}{I_{in}^2} \sum_n \frac{V_n^i}{1+j\lambda_n} \boldsymbol{J_n} \tag{2.64}$$

Recalling that $V_m = \langle f_m, \boldsymbol{E^i} \rangle$ and modal excitation coefficient $V_n^i = \langle \boldsymbol{J_n}, \boldsymbol{E^i} \rangle$, V_n^i can simply be calculated as:

$$V_n^i = V^T \boldsymbol{J_n} \tag{2.65}$$

By using this relation, input impedance simplifies to:

$$Z_{in} = -\frac{1}{I_{in}^2}\sum_n \frac{\left(V_n^i\right)^2}{1+j\lambda_n} \tag{2.66}$$

Each in the summation is considered as the modal impedance of the corresponding mode. When multiple modes are desired to be excited in an antenna with multiple feeds, the proper feed location for each mode can be chosen separately by utilizing this formulation.

2.4. Development of the Code

In this section, implementation steps of the MATLAB code which is developed for performing characteristic mode analysis of printed structures is presented.

As mentioned before, planar triangular surface patch model is used to discritize the surface of the conducting body. Fundamentally, the main objective of surface meshing is to obtain geometrical information (vertex coordinates, etc.) about triangular patches. Moreover, the mesh data file contains the connectivity information about vertices (nodes) and edges of each triangle.

In this work, the mesh data file is obtained from two different tools: PDE Toolbox [35] of MATLAB and the open-source version 2.10.1 of the mesh generator tool called GMSH [36]. Mesh generator tool of PDE Toolbox is suitable for planar two dimensional surfaces and it provides three arrays named as *p*, *e* and *t*. Cartesian coordinates *x* and *y* of the nodes are provided by array *p*, the row index of this array represents the node number. Node numbers for each triangle are provided by array *t*, the row index of this array represents the triangle number. Edge numbers including interior and boundary edges of the surface is provided by array *e*. However, this array is modified to exclude the boundary edges since RWG basis functions are defined only for interior edges. GMSH provides more flexible usage compared to PDE Toolbox since the meshing algorithm can be chosen and mesh size constraints on subdomains can be enforced. The mesh data output file is in a different format than the output file of PDE Toolbox. The code is first developed

to work with the output file (*p*, *t* and *e* arrays) of PDE Toolbox. Hence the mesh data obtained from GMSH is first converted to the output data format of PDE Toolbox to be compatible with the developed code.

The next step is to obtain node numbers and node coordinates for each interior edge. Geometric information of the interior edges is important because it is critical for defining RWG basis functions. Node numbers of each interior edge is obtained by developing a simple algorithm that first lists the node numbers of all edges, and then finds node numbers of the searched edge. Node coordinates for each interior edge are obtained by mapping elements of array *p* into another array properly. Note that the number of the interior edges is equal to the number of RWG basis functions. Thus, this number is also equal to *N* value which is the number of rows and columns of the square matrix *Z*, the length of the vectors *V* and *I* in equation (2.49).

A square patch with 18 triangular meshes is illustrated in Figure 5 as an example. The numbers with and without circles correspond to triangle numbers and edge (RWG) numbers, respectively.

Next, the length of interior edges and the area of triangles should be found. These parameters are computed easily by using node coordinates of triangles and edges. Calculation of MoM matrix entries requires coordinate information of centroid points for each triangle. These coordinates are derived by averaging the vertex coordinates of each triangle.

To complete the geometrical information about the RWG basis functions, plus and minus signs must be assigned to each triangle pair corresponding to each interior edge as shown in Figure 6. Assignment order of plus and minus signs to triangle pair is not important, but it should be kept in mind that the resultant current coefficients I_n's are calculated with respect to this order choice.

Note that on an interior triangle, 3 different RWG basis functions are defined. Consider triangle 10 as shown in Figure 6, this triangle is the negative triangle for RWG basis functions 12, 13 and 6.

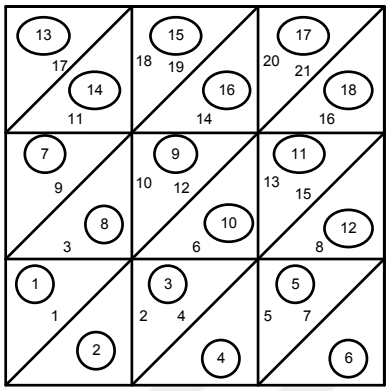

Figure 5 Triangulated square patch example

The possible assignments for triangle pairs of triangulated square patch example shown in Figure 5 are depicted in Figure 6 [41]

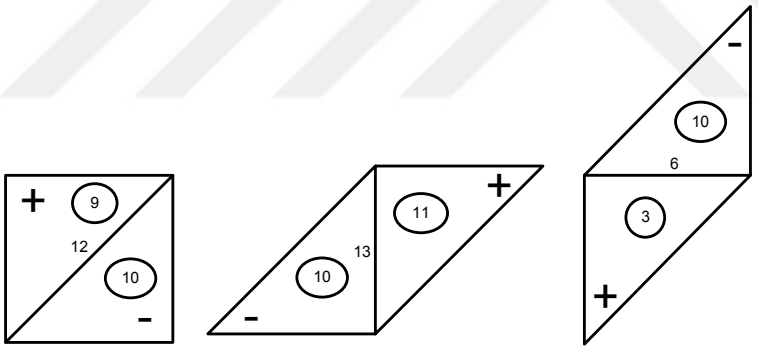

Figure 6 Triangle pairs of triangulated square patch example

MoM matrix entries (equation (2.50)) are computed by utilizing the MATLAB function, named as "impmet.m", developed by Makarov. Detailed information about the algorithm of this function is given in [41]. This function uses all geometric data obtained from the mesh generator tools and also the Green's function of the grounded dielectric slab. Therefore, prior to executation of this function, all geometric data of the primary triangles, secondary triangles and RWG basis functions; output parameters of the DCIM (complex distance and

coefficients corresponding to the dielectric constant and height of the substrate and the considered frequency) should be computed.

Note that the resultant MoM matrix should be symmetric since Galerkin's testing procedure is applied. This symmetry is lost during the numerical implementation since different integration rules are used for potential and testing integrals. However, when the symmetry of the MoM matrix is lost, eigenvalues becomes imaginary. Therefore, symmetry of the Z matrix is important for the accurate computation of the characteristic modes. Therefore, the resultant Z matrix is manipulated to make it symmetric by replacing each off-diagonal entry of the matrix with the arithmetic mean of the values obtained for Z_{mn} and Z_{nm}.

After obtaining the symmetric Z matrix, characteristic mode analysis is performed. In order to evaluate eigenvalues and eigenvectors from equation (2.24) real and imaginary parts of Z matrix, R and X, are obtained. Then, "eig" command in MATLAB is used with R and X: "$[EVEC, EVAL] = eig(X, R)$". $EVEC$ is a diagonal matrix with the eigenvalues on the diagonal, $EVAL$ is a full matrix whose columns are the corresponding eigenvectors [33]. Depending on the properties of R and X, the most suitable algorithm for computing eigenvalues is selected automatically by MATLAB [5]. Each eigenvalue and the corresponding eigenvector determine each characteristic mode at the specified frequency.

Then, modal significance (MS) of each mode is computed. Recall that MS values are less than or equal to 1. MS values are sorted in descending order to number the modes according to their dominancies. The characteristic mode whose MS value is the largest is the dominant mode and called as the 1^{st} *mode*. Next one is called the 2^{nd} *mode*, and so on. Hence, while MS value decreases, mode number increases.

CHAPTER 3

NUMERICAL RESULTS

In this chapter, the numerical results obtained from the analysis of three different antenna structures are presented and discussed. First of all, a simple rectangular patch is analyzed to verify the proper operation of the developed code. Then, the characteristic mode analysis of an ultra wide band planar bevel-shaped quasi-monopole antenna is performed to demonstrate the performance of the developed code for more complex structures within a large frequency bandwidth. The results obtained from the developed code are compared with the results obtained by using a commercially available electromagnetic simulation software called FEKO. Finally, a rectangular microstrip patch antenna is considered as the printed structure. The analysis of the microstrip antenna requires the use of the Green's function in layered media. For the rectangular patch antenna in addition to the characteristic mode analysis, input impedance calculations for different coaxial probe feed locations are also performed by using the obtained characteristic modes. The input impedance analysis could guide an antenna engineer during the design process for the proper choice of the feed location.

3.1. Analysis of Rectangular Patch

In this section, the results obtained from scattering analysis and characteristic mode analysis of a rectangular conducting patch of length 6 cm and width 4 cm are presented. In the first part of this section, the MoM analysis of the rectangular patch is performed for incident electric fields with different polarizations and the resultant current distributions on the patch are presented. The purpose of this

analysis to verify the proper construction of the *Z* matrix and *V* vector by using the developed code. In the second part, characteristic mode analysis is carried out for the same rectangular conducting patch and corresponding eigenvalues, MS values and current distributions of each characteristic mode are presented.

The rectangular patch is located in *xy-plane*. The operating frequency is 2.4 GHz which is the first resonance frequency of this structure [5]. MATLAB PDE Toolbox is used to generate mesh data file of the rectangular patch. A uniform mesh is obtained with 512 right triangles and 736 RWG basis functions. The same mesh structure is used for both scattering and characteristic mode analysis.

3.1.1. Scattering Analysis

The current distribution on the rectangular conducting patch for *x-polarized*, *y-polarized* and *xy-polarized* normally incident electric fields are shown in Figure 7, Figure 8 and Figure 9, respectively.

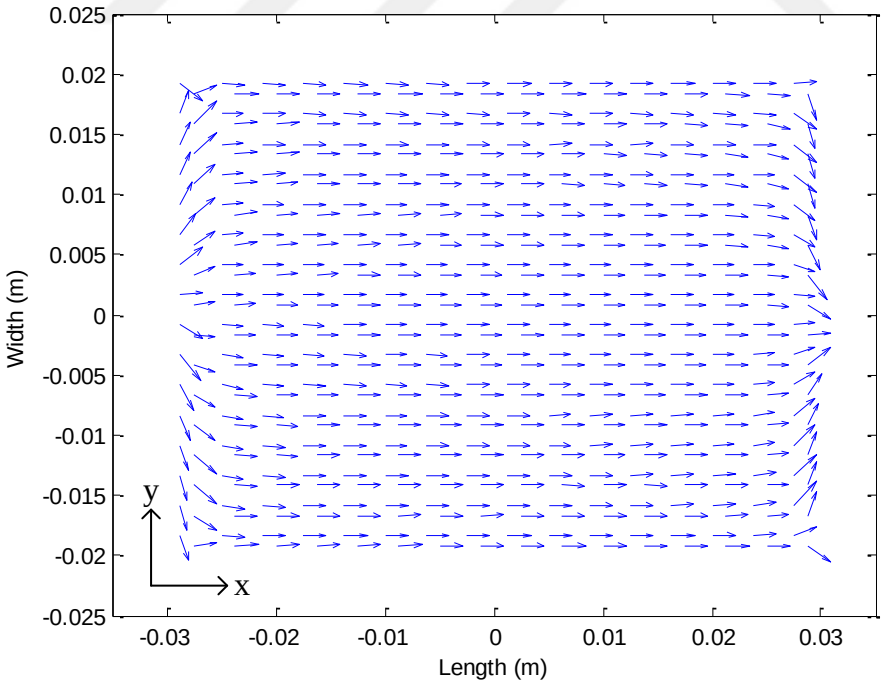

Figure 7 Current distribution for x-polarized incident electric field

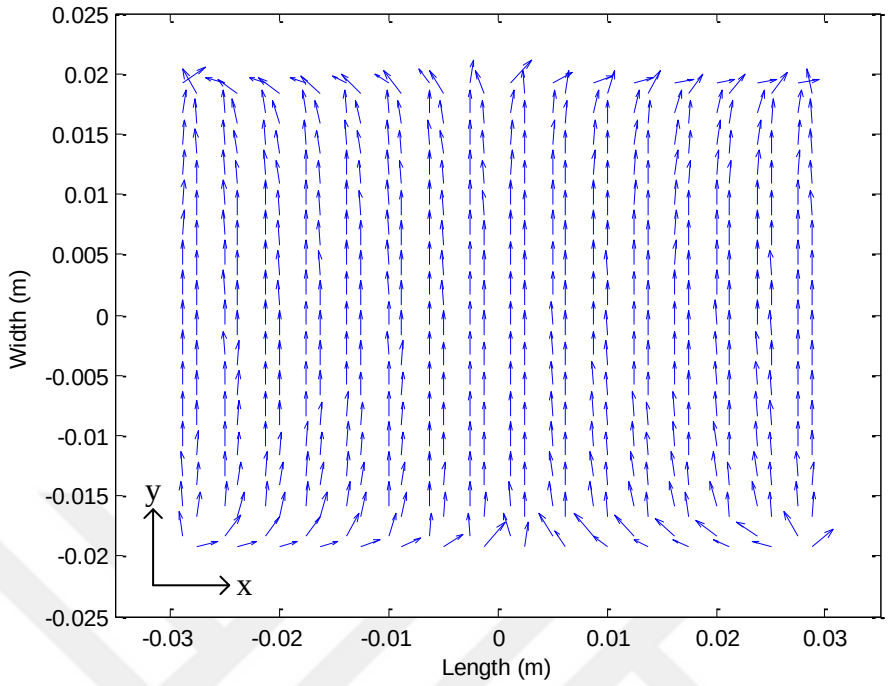

Figure 8 Current distribution for y-polarized incident electric field

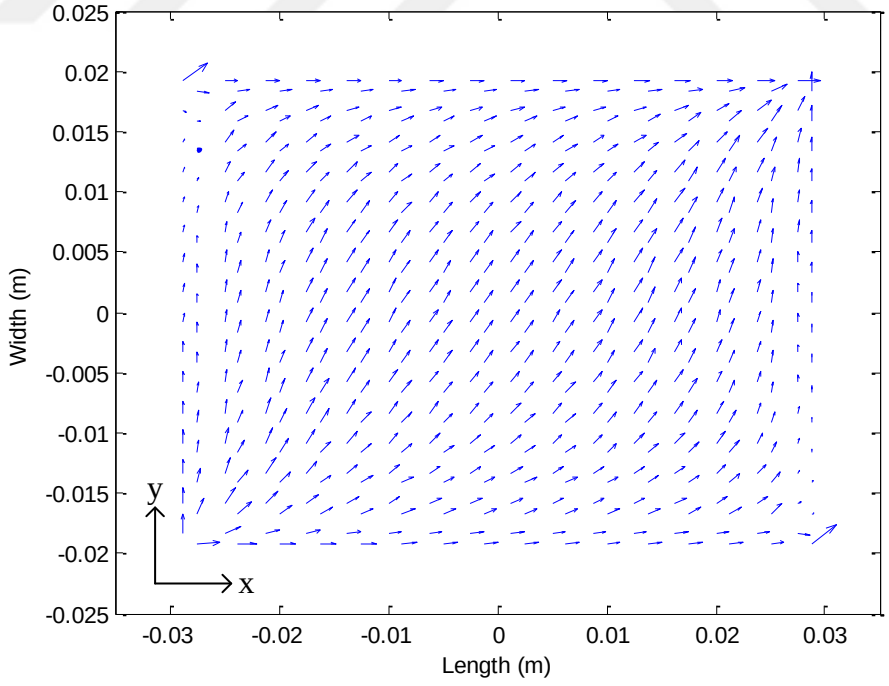

Figure 9 Current distribution for xy-polarized incident electric field

Note that, magnitude of current vectors are normalized to maximum magnitude on the patch, in order to make all current vectors more visible so that the current pattern on the surface can be seen clearly.

As it is expected and observed in Figure 7, Figure 8 and Figure 9, surface current on the rectangular conducting patch aligns with the direction of the incident electric field. These results demonstrate that MoM matrix and excitation vector are computed accurately by using the developed code. Therefore, the developed code is ready to be used for characteristic mode analysis.

3.1.2. Characteristic Mode Analysis

In this part, the characteristic mode analysis is carried out for the rectangular conducting patch at 2.4 GHz. As mentioned before, this frequency is the first resonance frequency of this structure. Eigenvalues and eigenvectors corresponding to each characteristic mode are obtained by solving equation (2.24). Obtained eigencurrent distributions are compared with the results presented in [5]. Both in [5] and in this work, modes are ordered according to their modal significance values, except the capacitive mode J_0.

The current distributions for the first 6 characteristic modes are presented in [5] as illustrated in Figure 10.

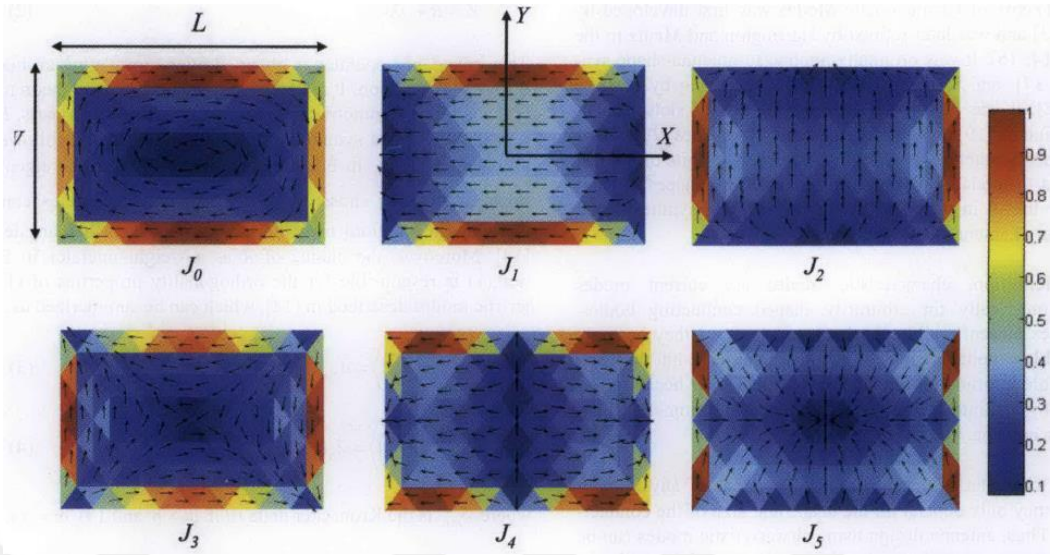

Figure 10 Current distributions presented in [5]

The mode current distributions obtained by the developed code for J_0, J_1, J_2, J_3, J_4 and J_5 are presented in Figure 11, Figure 12, Figure 13, Figure 14, Figure 15 and Figure 16, respectively.

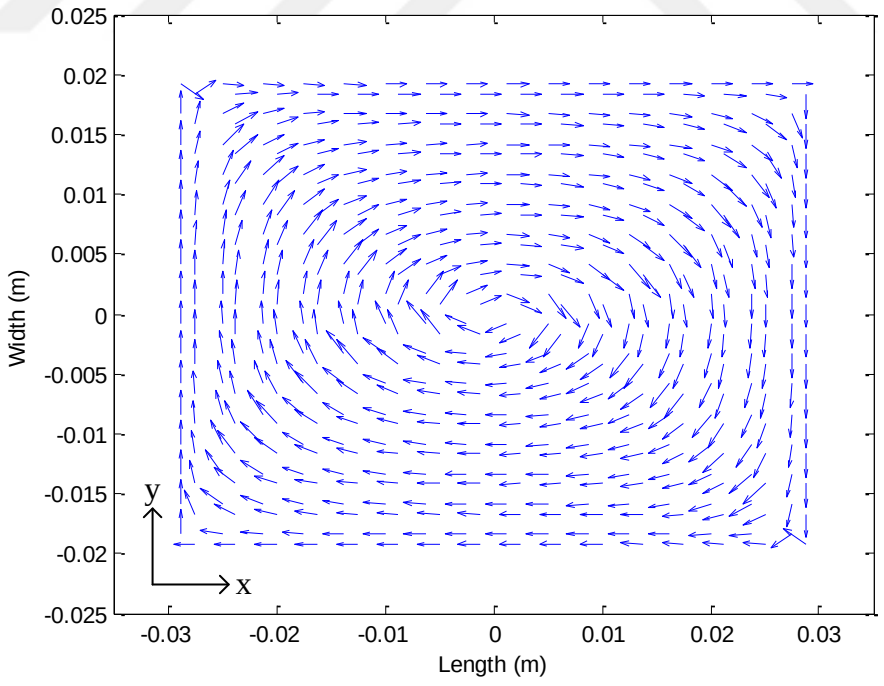

Figure 11 Current distribution for J_0

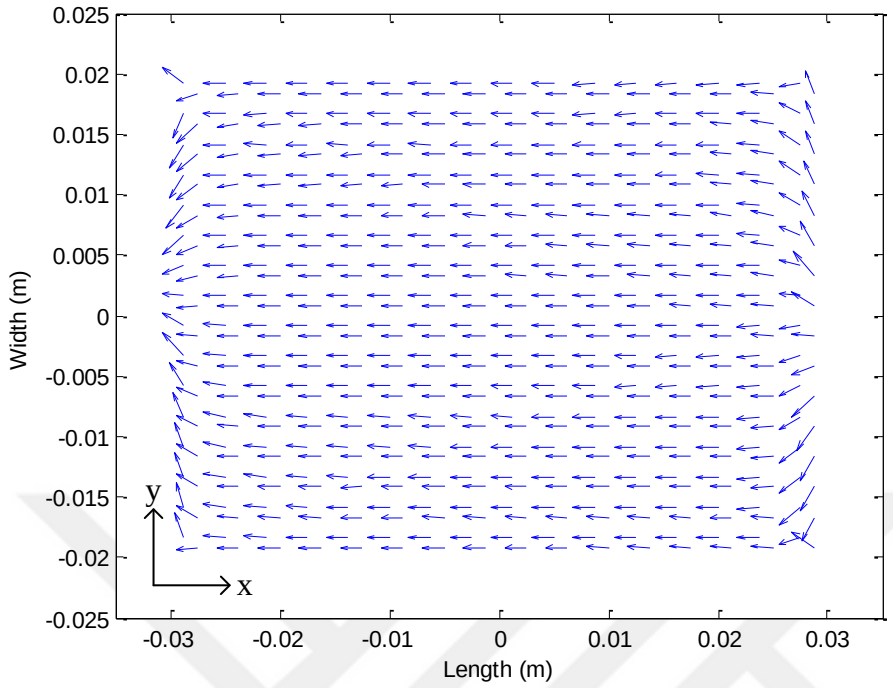

Figure 12 Current distribution for J_1

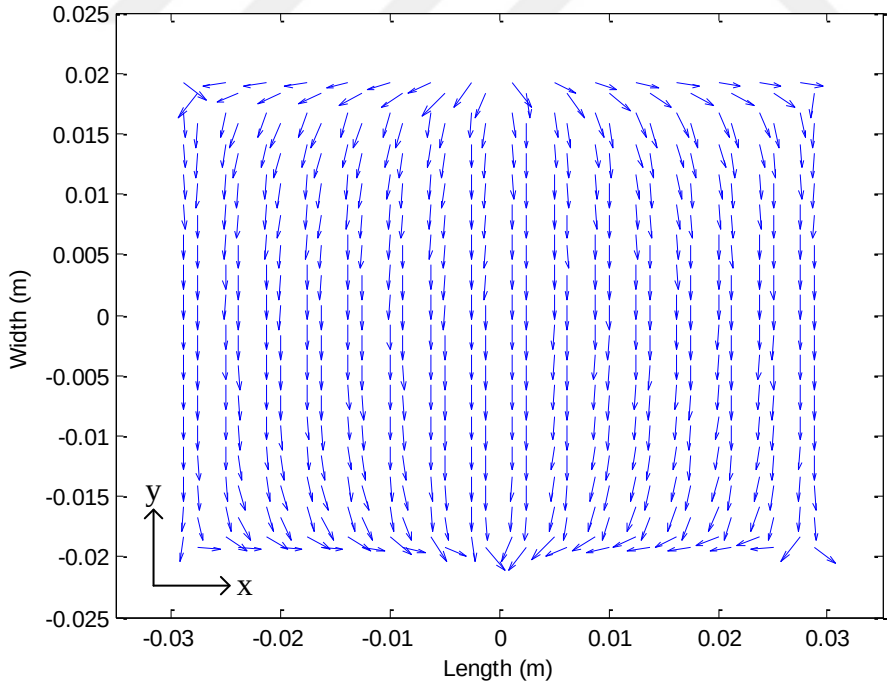

Figure 13 Current distribution for J_2

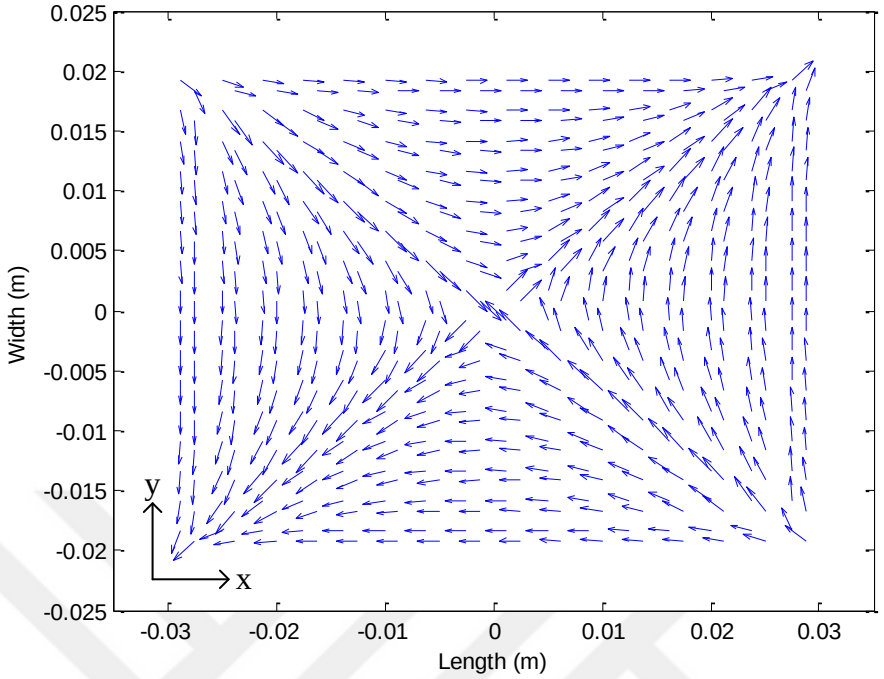

Figure 14 Current distribution for J_3

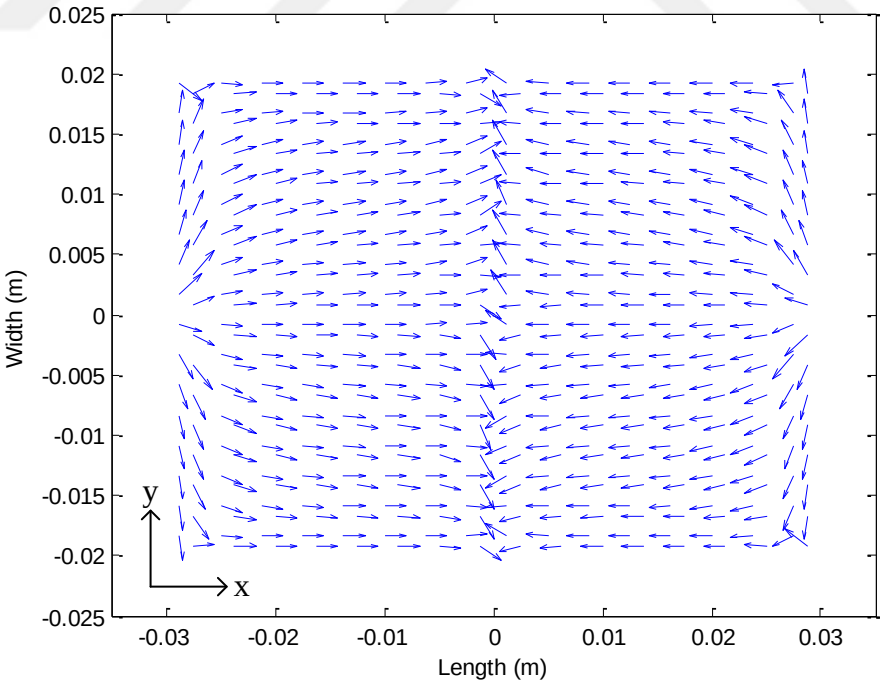

Figure 15 Current distribution for J_4

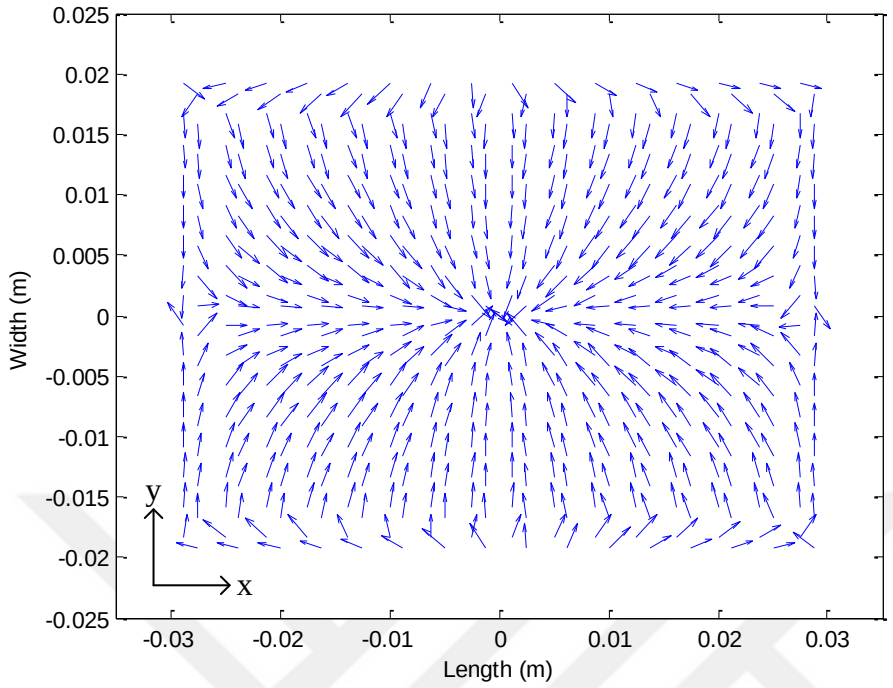

Figure 16 Current distribution for J_5

By comparing Figure 10 and Figure 11 through 16, the good agreement between the results can be observed. As suggested in [5], the mode current distributions can be represented by simple schematics as shown in Table 1. Eigenvalue and MS value of each mode are also included in the table.

As discussed in Chapter 2, the modes with positive eigenvalues were inductive modes. J_0 mode has positive eigenvalue and the loop like current schematic of J_0 also supports that it is an inductive mode. For J_1, even though the eigenvalue is positive, it can not be classified as inductive mode, since when the eigenvalue is close to zero, the sign of it might be erroneous due to numerical errors. Hence, it is better to classify it as resonant mode. Finally, J_2, J_3, J_4 and J_5 are capacitive modes (negative eigenvalues) which can also be observed from their current schematics.

Table 1 Current schematics of the modes

Mode	Current Schematic	Eigenvalue	MS
J_0	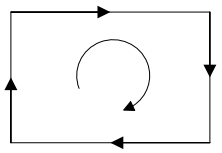	5.0905	0.1928
J_1	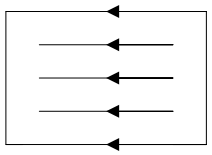	0.0241	0.9997
J_2	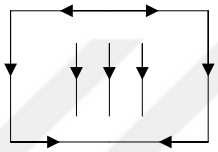	-1.3226	0.6031
J_3	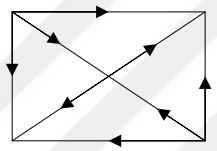	-8.6451	0.1149
J_4	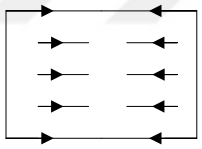	-19.6047	0.0509
J_5	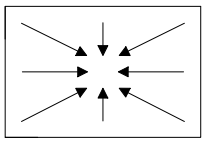	-132.1719	0.0076

Modal excitation coefficients V_n^i of these modes for *x-polarized*, *y-polarized* and *xy-polarized* incident electric fields are shown in Table 2.

Table 2 Modal excitation coefficients of the modes

Mode	**MS**	V_n^i ***(x-polarized)***	V_n^i ***(y-polarized)***	V_n^i ***(xy-polarized)***
J_0	0.1928	-3.9302 x 10^{-19}	-1.9651 x 10^{-19}	-6.1664 x 10^{-19}
J_1	0.9997	-8.9749 x 10^{-4}	1.325 x 10^{-5}	-8.8424 x 10^{-4}
J_2	0.6031	-1.072 x 10^{-5}	-9.565 x 10^{-4}	-9.6722 x 10^{-4}
J_3	0.1149	2.4395 x 10^{-19}	-1.7347 x 10^{-18}	-1.5179 x 10^{-18}
J_4	0.0509	5.9292 x 10^{-19}	2.7444 x 10^{-19}	8.6059 x 10^{-19}
J_5	0.0076	-1.6263 x 10^{-18}	1.0842 x 10^{-18}	-5.0144 x 10^{-19}

As discussed in Chapter 2, modal significance and modal excitation coefficient V_n^i are factors that determine how strongly a mode will be excited. As shown in Table 2, absolute values of modal excitation coefficients of the modes J_0, J_3, J_4, J_5 are much smaller than the other modes for three cases, since the incident electric fields are linearly polarized. However, the modes J_1 and J_2 are important modes according to modal excitation coefficients for these three incident electric fields. As shown in Figure 12 and Figure 13, the mode currents of J_1 and J_2 are aligned to *x*-direction and *y*-direction, respectively. Therefore, for *x-polarized* incident electric field, absolute value of modal excitation coefficient of J_1 is greater than J_2. For *y-polarized* incident electric field, absolute value of modal excitation coefficient of J_2 is greater than J_1, even though MS value of J_1 is greater than J_2. This situation demonstrates that modal excitation coefficients gives information about excitation strength of the characteristic modes independently of MS values. For *xy-polarized* incident field, absolute value of modal excitation coefficient of J_1 and J_2 are closer to each other, whereas the mode currents of each mode have the same stances according to *xy-polarized* incident electric field.

The developed code is verified for the characteristic mode analysis, it can be used to perform characteristic mode analysis of arbitrary shaped conducting surfaces. This ability of the code is proven in the following section by analyzing the bevel-shaped antenna.

3.2. Characteristic Mode Analysis of the Bevel-Shaped Antenna

In this section, the characteristic mode analysis results of the ultra wide band printed planar bevel-shaped quasi-monopole antenna structure (shown in Figure 17) obtained by using the developed code and by using the commercial electromagnetic simulator FEKO are presented and compared. This antenna structure is proposed and studied in [47].

The operating frequency band of this antenna is from 3 GHz to 11 GHz, so characteristic mode analysis is performed within this band. 81 frequency points are chosen with 100 MHz step size.

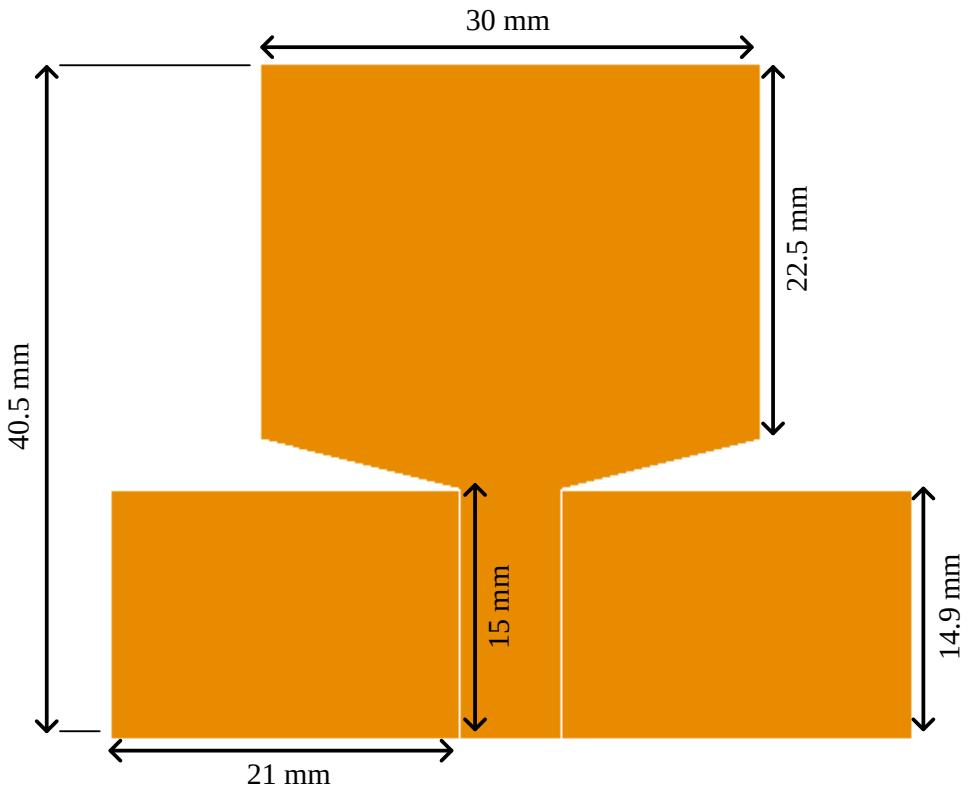

Figure 17 Bevel-shaped antenna geometry

Meshed surface in FEKO contains 773 triangles as illustrated in Figure 18. For the developed code, this structure is meshed by using GMSH. Meshed surface in GMSH contains 586 triangles as illustrated in Figure 19.

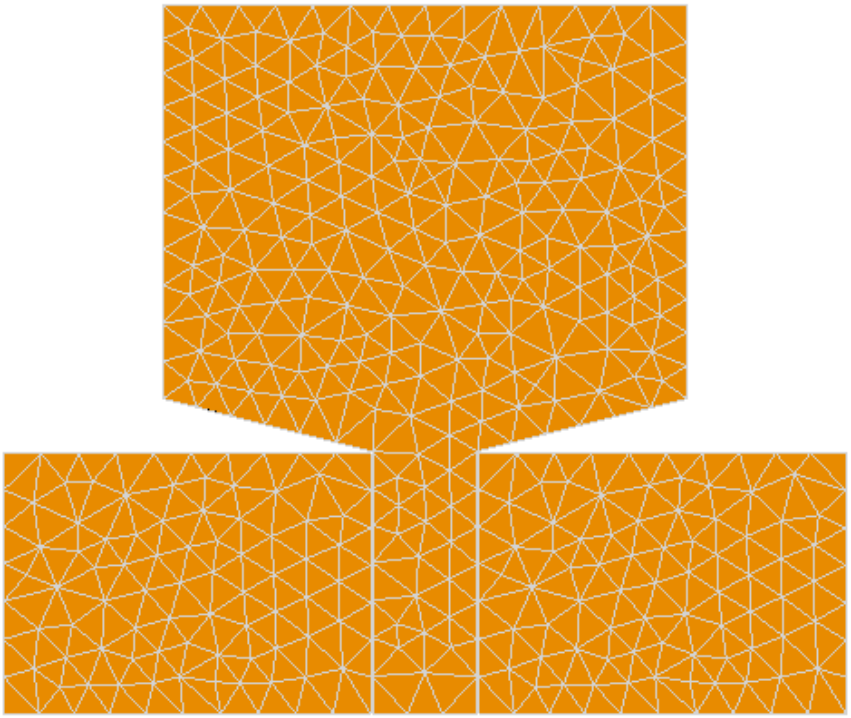

Figure 18 Meshed structure in FEKO

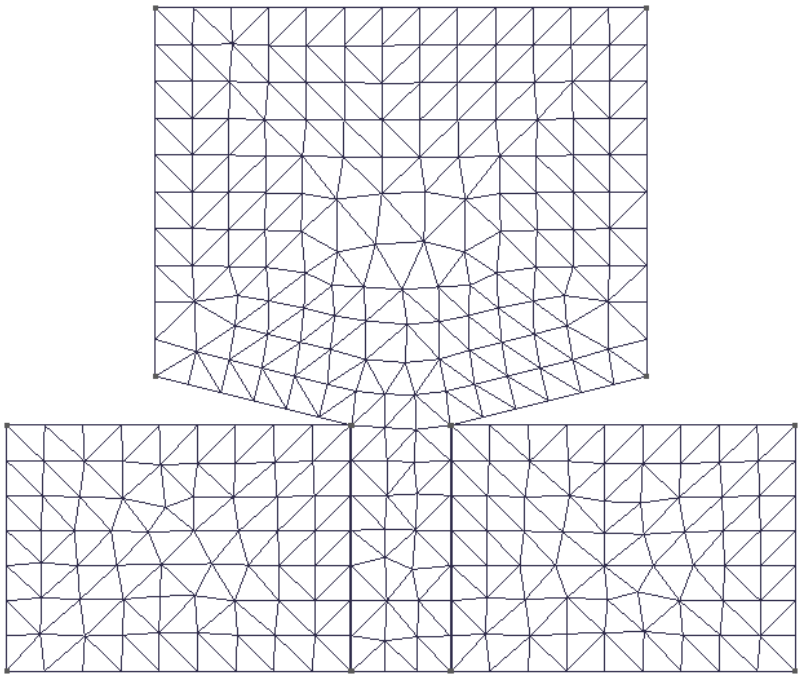

Figure 19 Meshed structure in GMSH

The variation of eigenvalues and corresponding MS values with respect to frequency is calculated by using FEKO and by using the developed code.

Eigenvalue and corresponding MS value results for the first interested characteristic mode are presented and compared in Figure 20 and Figure 21, respectively. It can be observed that no eigenvalues found after 7 GHz. It means this mode is not excited at corresponding frequencies. Similar comparisons for the second mode are presented in Figure 22 and Figure 23. Finally, Figure 24 and Figure 25 illustrates the comparison for the third mode.

From these figures, a good agreement between the results obtained by FEKO and the developed code can be observed. Note that, around 4.2 GHz a mode transition occurs for the third mode but FEKO considers the mode which occurs before 4.2 GHz and the mode which occurs after 4.2 GHz to be the same modes. That is the reason of the discrepancy in the results for the third mode.

It can be concluded that each mode is dominant within different frequency bands. For example, the first mode is dominant around 3.2 GHz whereas the second mode is dominant around 6.5 GHz. This multi-mode characteristics makes this bevel-shaped monopole a wideband antenna.

To analyze the distribution of mode currents, 5 GHz is chosen as the frequency of interest since both of the modes have similar MS values at this frequency. Eigencurrents obtained by FEKO are plotted in Figure 26, Figure 27 and Figure 28 for the first, second and third modes, respectively.

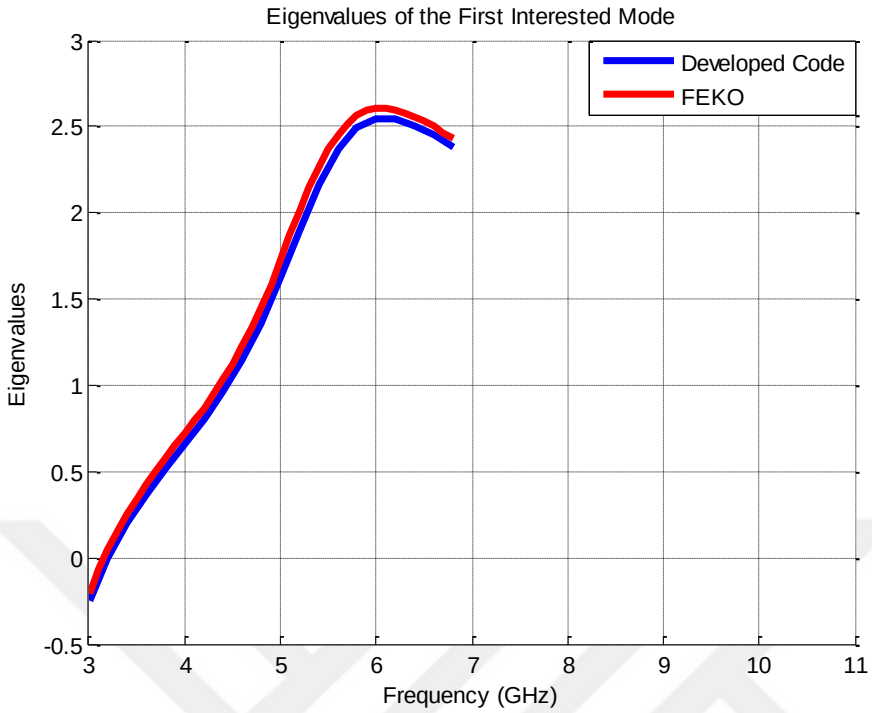

Figure 20 Eigenvalues of the 1st interested mode

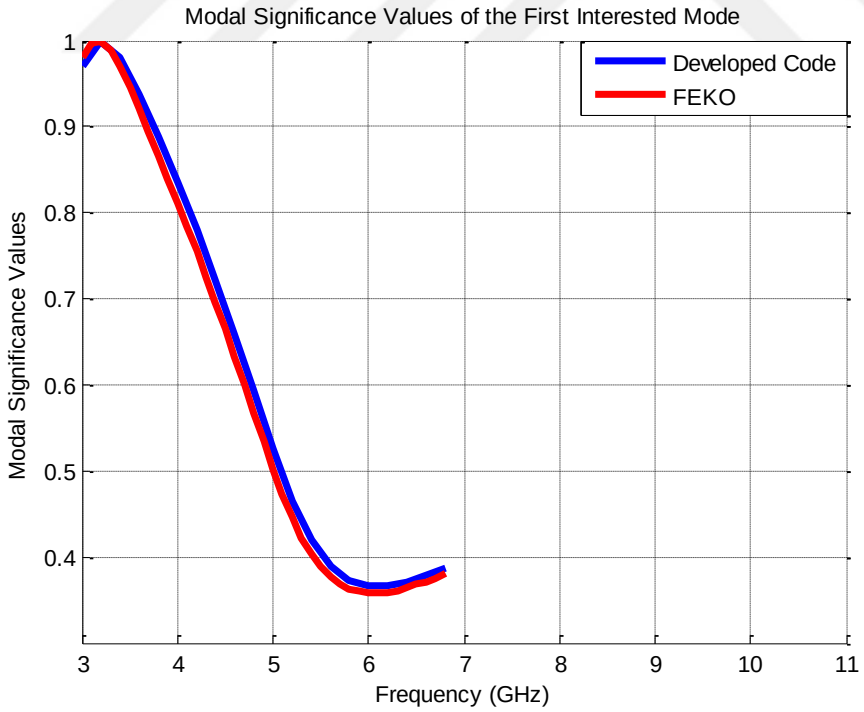

Figure 21 MS values of the 1st interested mode

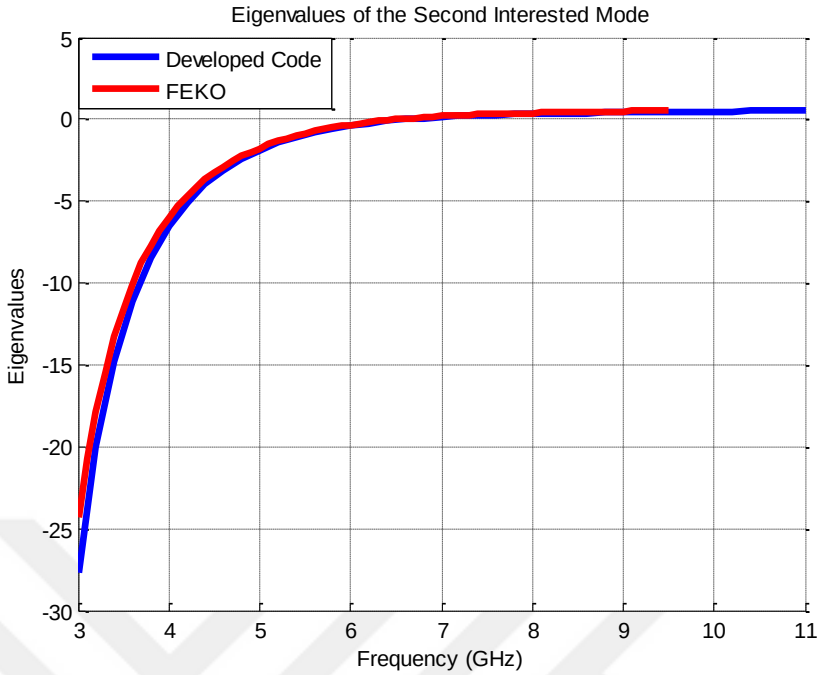

Figure 22 Eigenvalues of the 2nd interested mode

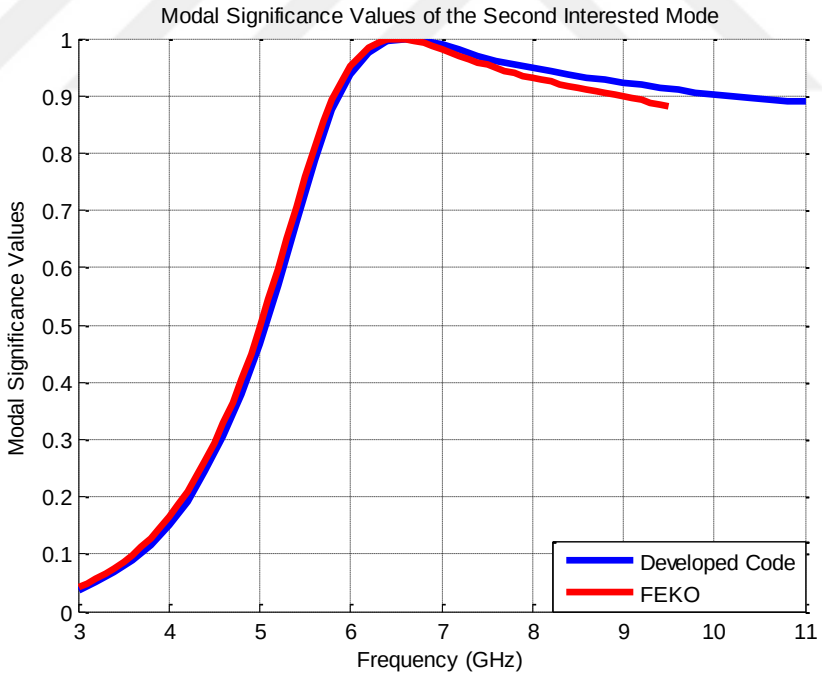

Figure 23 MS values of the 2nd interested mode

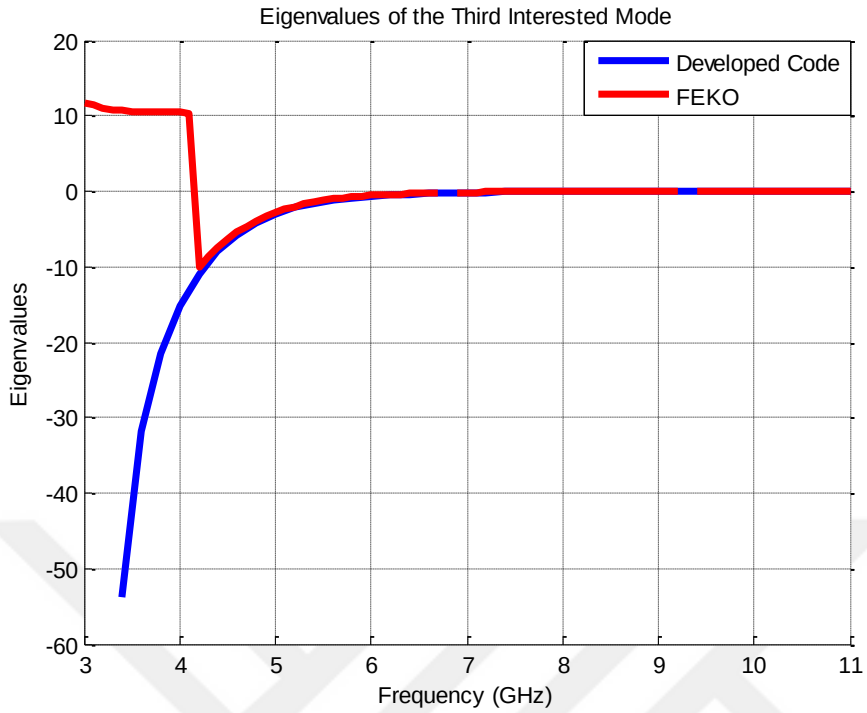

Figure 24 Eigenvalues of the 3rd interested mode

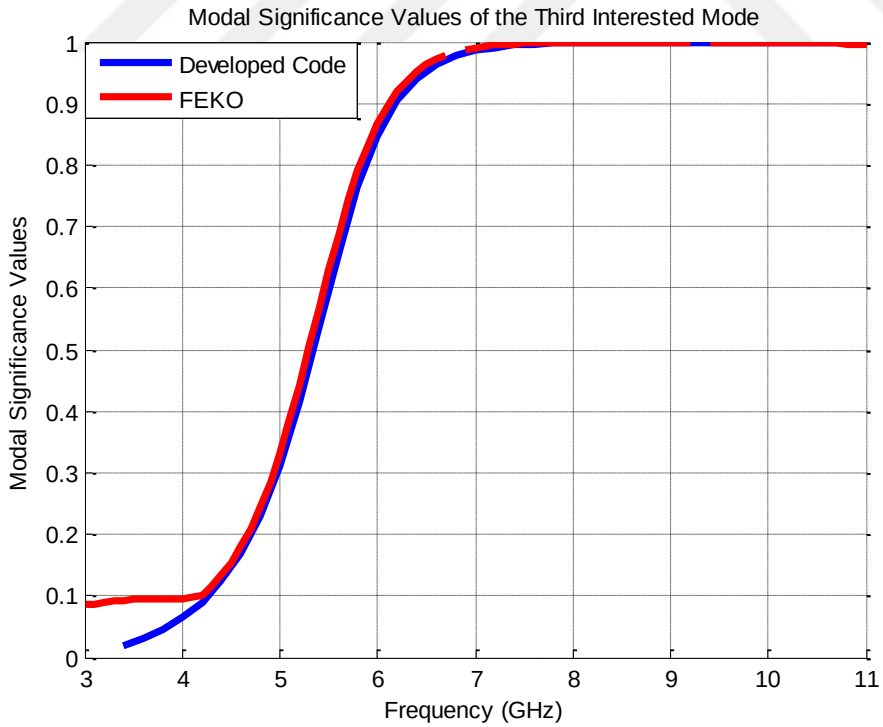

Figure 25 MS values of the 3rd interested mode

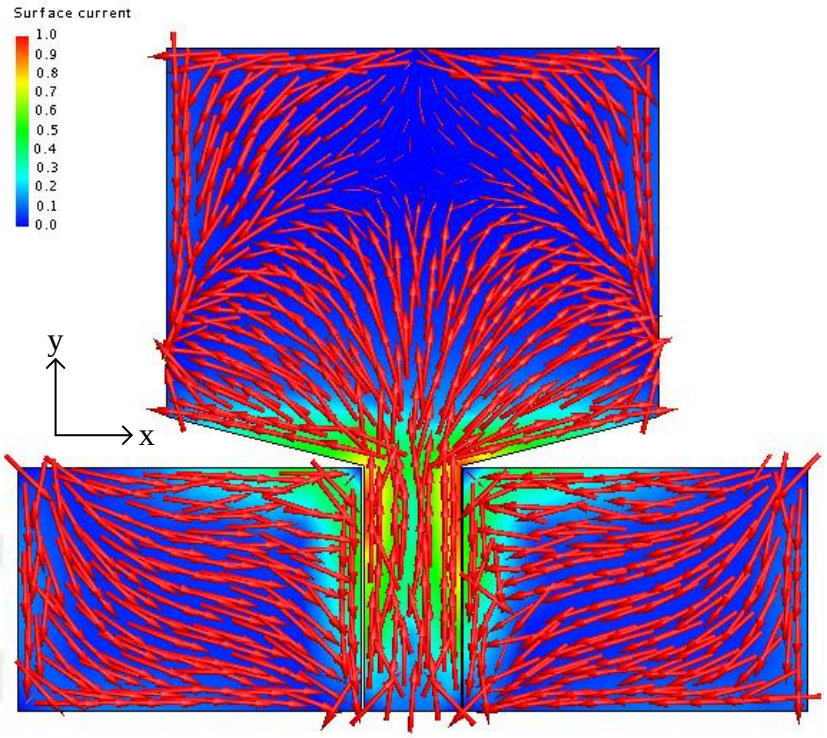

Figure 26 Current distribution of the 1st interested mode obtained from FEKO

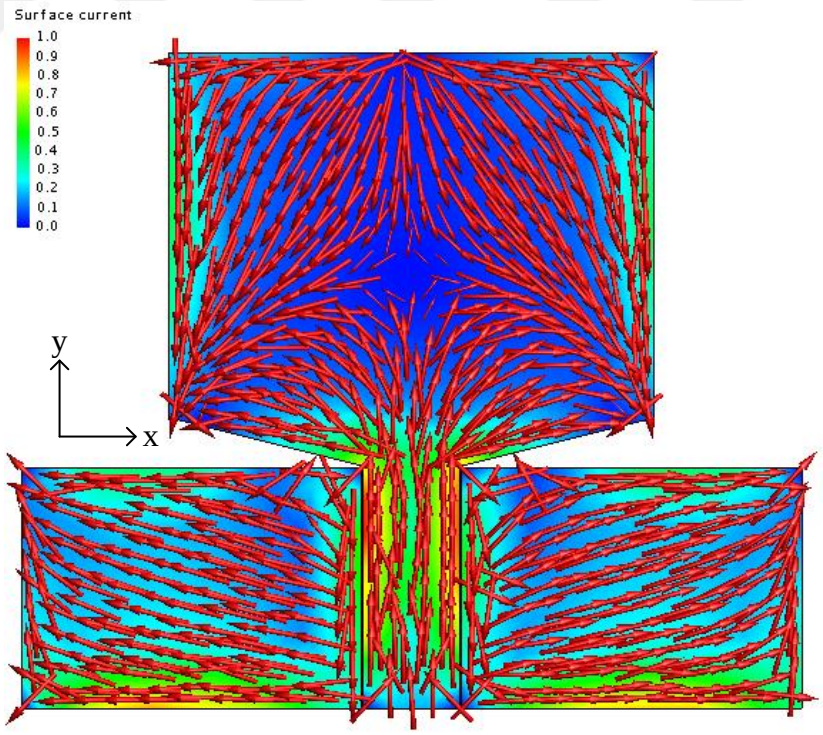

Figure 27 Current distribution of the 2nd interested mode obtained from FEKO

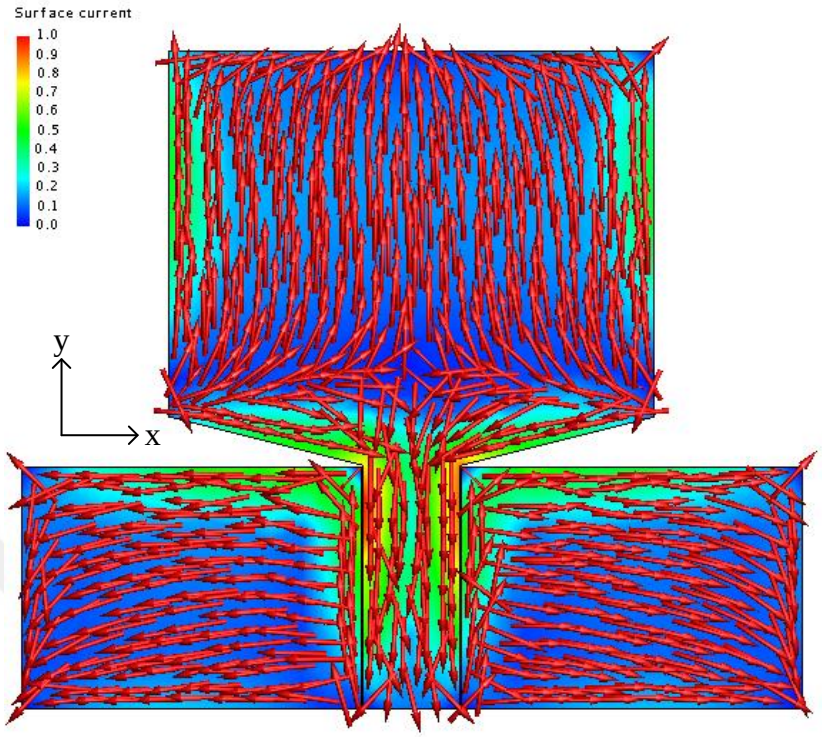

Figure 28 Current distribution of the 3rd interested mode obtained from FEKO

Figure 29, Figure 30 and Figure 31 illustrates the distribution of mode currents obtained by the developed code. Comparison of the corresponding figures (for example, Figure 26 and Figure 29) verifies that the modes considered by FEKO and by the developed code are the same modes. The first mode experiences a phase change at a point closer to the edge of the monopole whereas this phase change occurs closer to the feed point for the second mode. This may be the reason why the first mode has a resonance frequency smaller than the second mode.

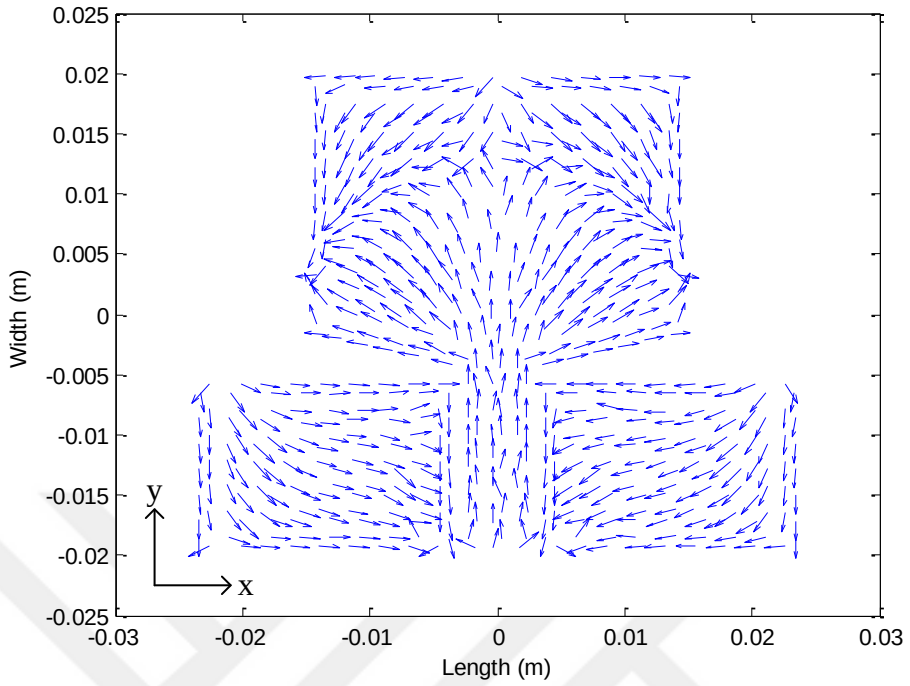

Figure 29 Current distribution of the 1st interested mode obtained from code

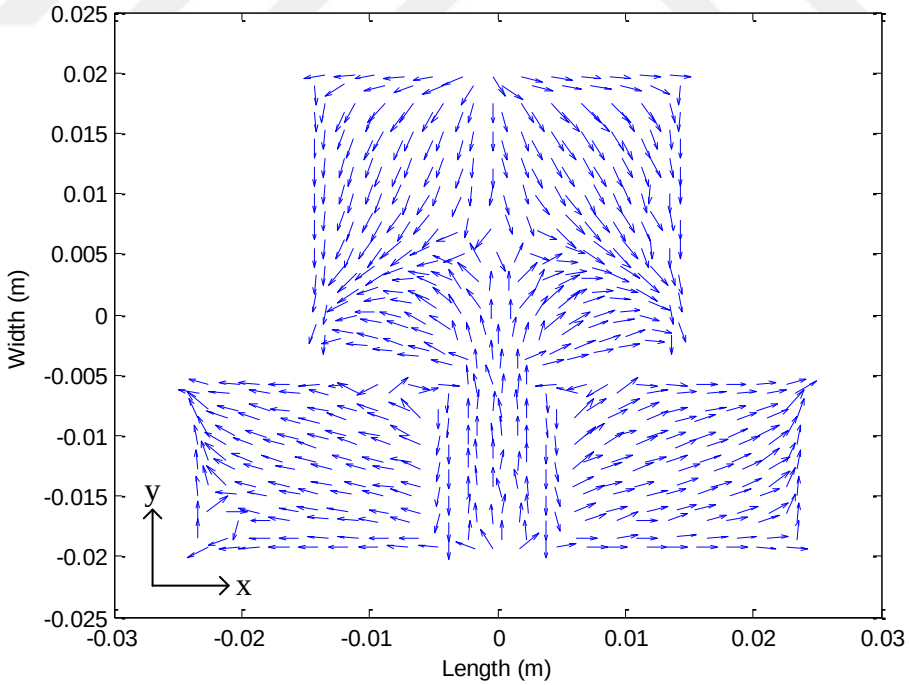

Figure 30 Current distribution of the 2nd interested mode obtained from code

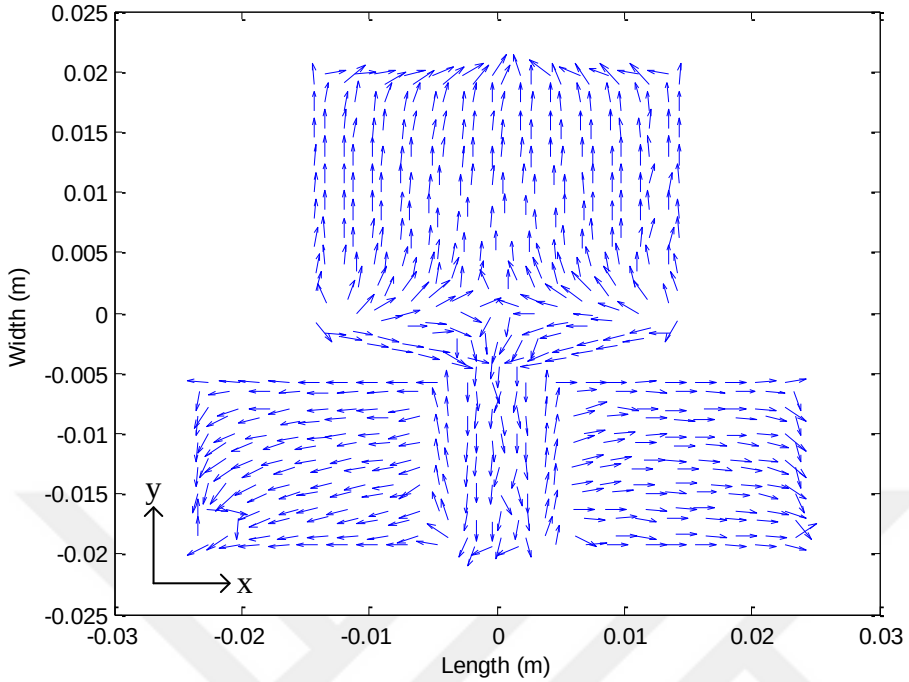

Figure 31 Current distribution of the 3rd interested mode obtained from code

The results of characteristic mode analysis for the bevel-shaped antenna structure demonstrate that analysis can be made successfully for arbitrarily shaped patches by using the developed code.

3.3. Analysis of Rectangular Microstrip Patch Antenna

In this section, the results obtained from characteristic mode analysis of the rectangular microstrip patch antenna structure by using the developed code are presented and discussed. This antenna structure consists of conducting patch (30mm x 25mm) on the top, the ground plane on the bottom, and the dielectric substrate between them. The conducting patch and the ground plane are assumed to be perfect dielectric conductors. The dielectric substrate is selected as commercially available RT/duroid 6002 high frequency laminate [48] from Rogers Corporation. Dielectric constant and thickness of this substrate are 2.94

and 1.524 mm, respectively. The frequency band is chosen to be between 2.1 GHz and 4.0 GHz for the analysis.

Analysis of this structure consists of two parts. First part includes eigenvalue and modal significance computations with respect to each characteristic mode within interested frequency band. Distribution of mode currents are obtained at a sample frequency. Note that antenna structure do not have any feeding mechanism in this part.

In the second part, a coaxial probe feed is considered for the antenna. This part involves input admittance computations with respect to different feed positions. This analysis provides an intuition about the optimum choice of the feed location. Note that the input admittance calculations are performed by using the characteristic modes as discussed in Chapter 2. In both parts, all analysis results are compared with FEKO and discussed.

3.3.1. Observation of the Characteristic Modes

In this part, characteristic modes and related parameters of the antenna structure are observed and discussed. As mentioned before, feeding mechanism does not exist for this analysis. First, eigenvalues and MS values are computed by using the developed code for the first two dominant modes and compared with the same parameters obtained by using FEKO at the interested frequency band.

The rectangular microstrip patch antenna structure is meshed by using PDE Toolbox. There are 264 triangles and 377 RWG elements on the meshed structure which is illustrated in Figure 32.

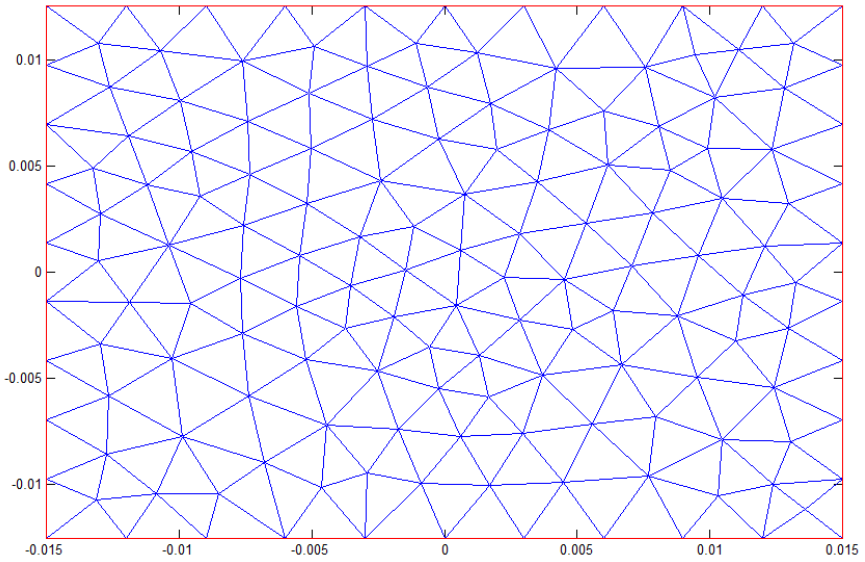

Figure 32 2D meshed antenna structure without feeding in PDE Toolbox

The meshed structure in FEKO is shown in Figure 33 and it has 232 triangles.

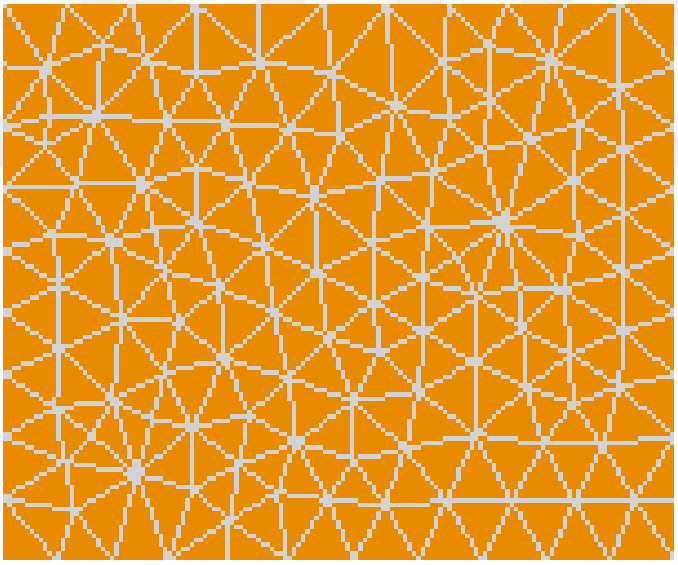

Figure 33 2D meshed antenna structure without feeding in FEKO

Eigenvalues and the corresponding MS values of the first mode obtained by using the developed code and by using FEKO are shown in Figure 34 and Figure 35, respectively.

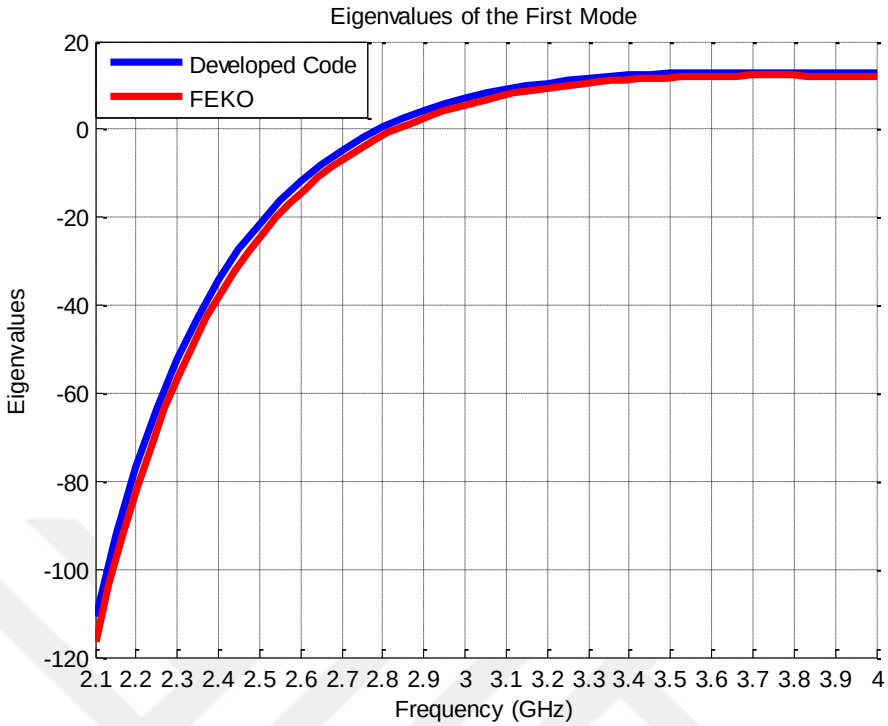

Figure 34 Eigenvalues of the 1st mode of antenna structure

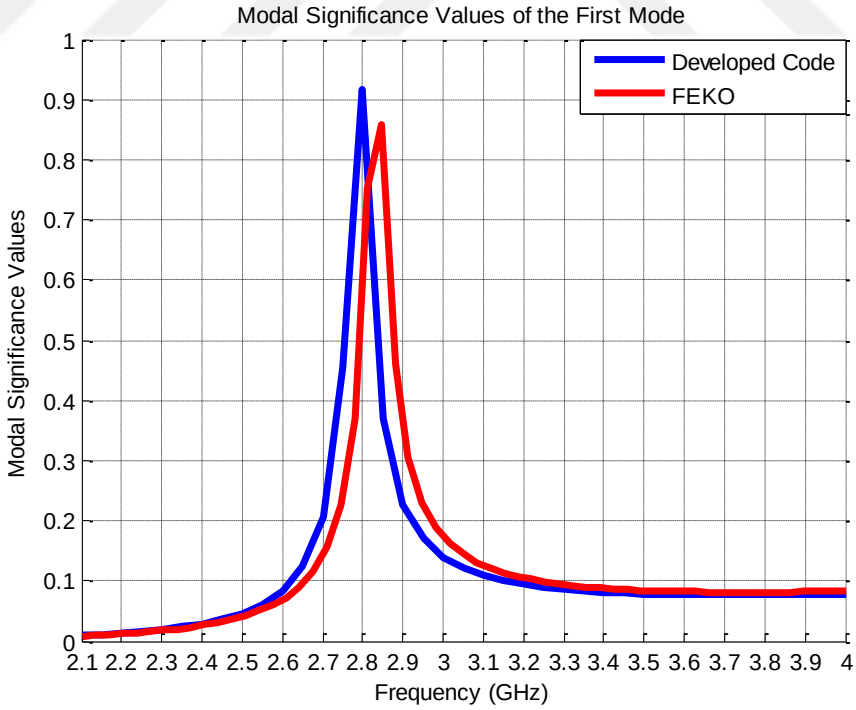

Figure 35 MS values of the 1st mode of antenna structure

As shown in Figure 34 and Figure 35, the results obtained by FEKO and by the developed code are in good agreement except for a slight shift in the resonance frequency. This shift may be due to the DCIM approximation used during the computation of the Green's functions in layered media. It is clear that the resonance frequency of the first mode is around 2.8 GHz. Observation of current distribution of the first mode is meaningful at the resonance frequency. Current distribution on the conducting patch of the antenna structure for the first mode is obtained at 2.8 GHz by using the developed code and by using FEKO; these current distributions are illustrated in Figure 36 and Figure 37, respectively.

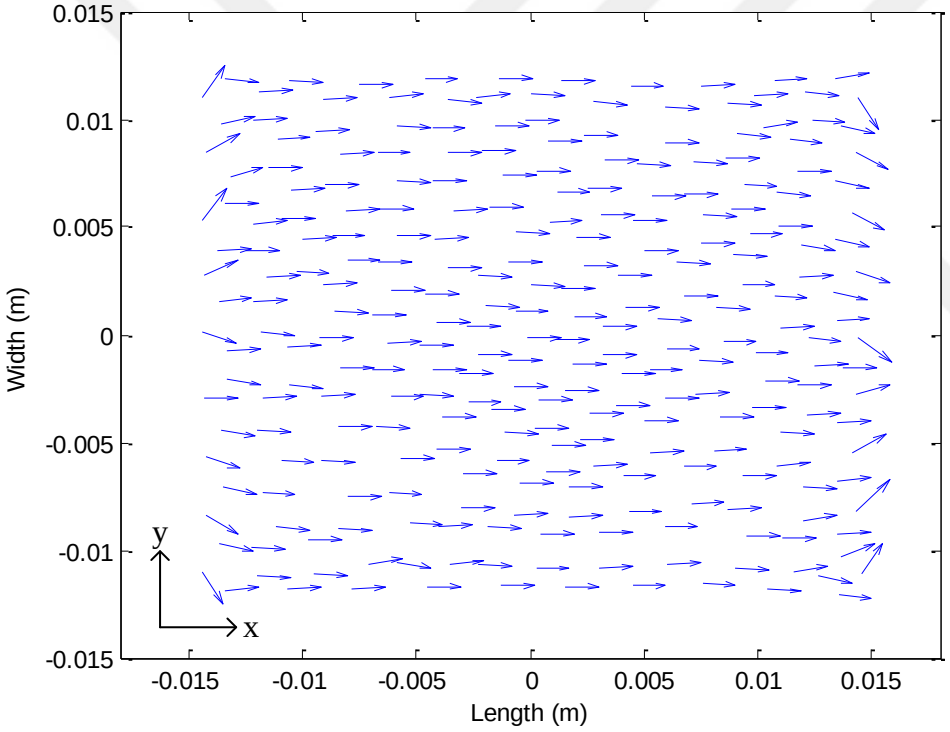

Figure 36 Current distribution of the 1st mode obtained by code

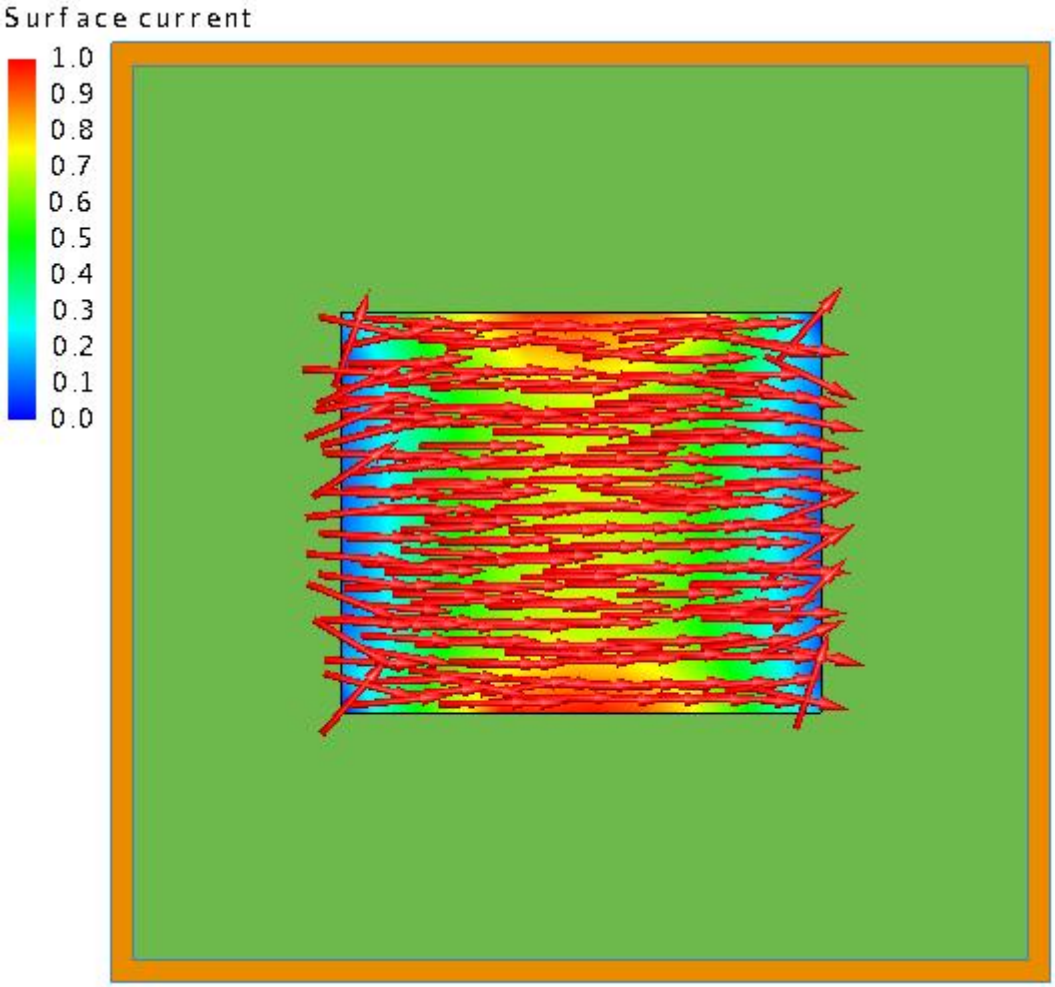

Figure 37 Current distribution of the 1st mode obtained by FEKO

As shown in Figure 36 and Figure 37, currents are aligned in *x*-direction, hence this mode can be called as the horizontal mode.

All computations made for the first mode are made for the second mode. Eigenvalues and MS values of the second mode obtained by using the developed code and by using FEKO is shown in Figure 38 and Figure 39, respectively.

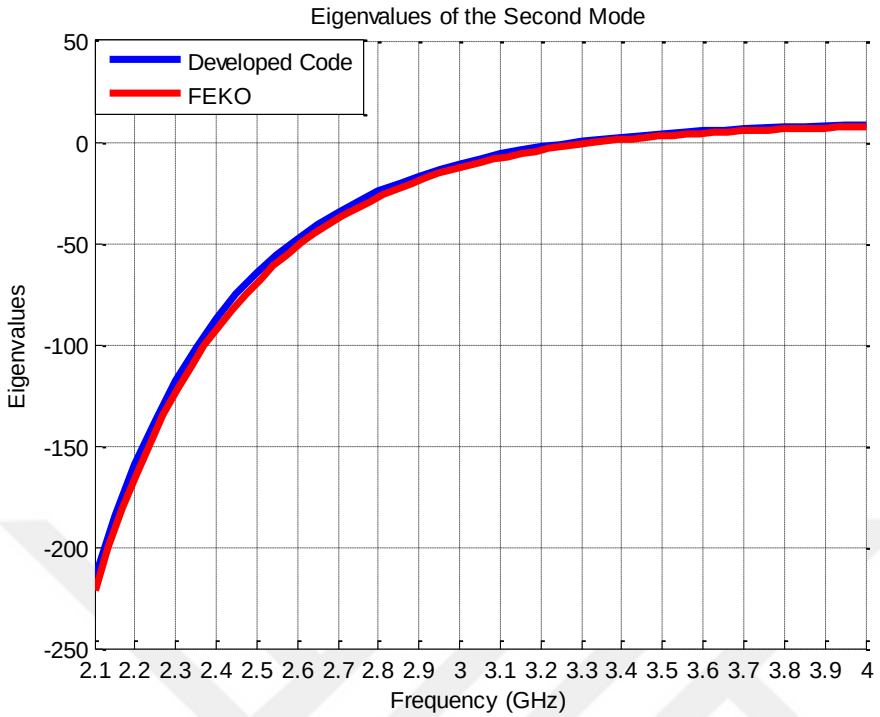

Figure 38 Eigenvalues of the 2nd mode of antenna structure

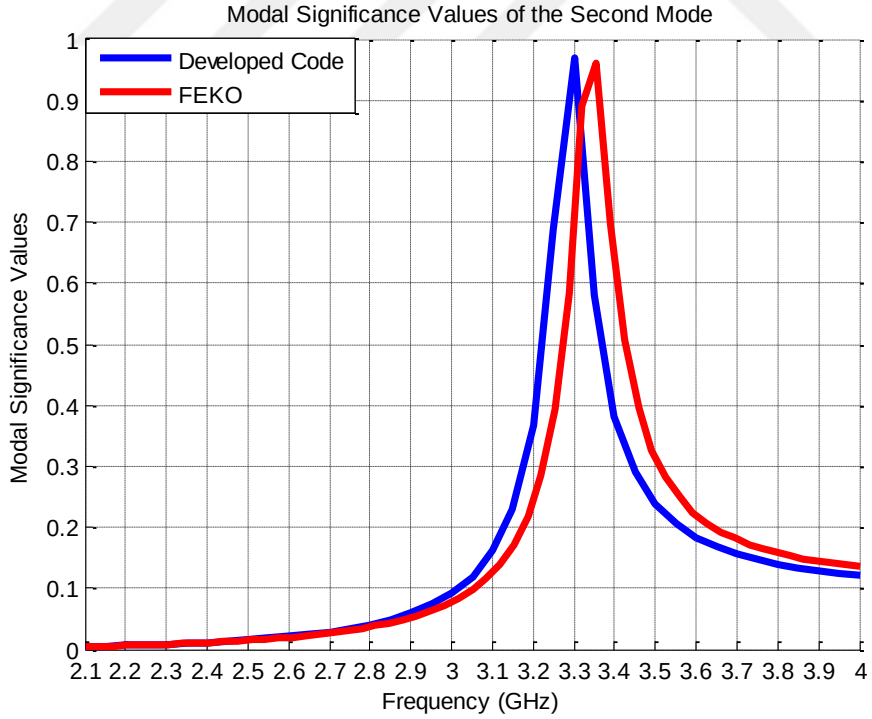

Figure 39 MS values of the 2nd mode of antenna structure

A similar frequency shift is observed in Figure 39, but the resonance frequency of the second mode can be considered as 3.3 GHz. Current distribution of the second mode is observed at this frequency. For the second mode, current distribution on the conducting patch obtained at 3.3 GHz by using the developed code and by using FEKO are illustrated in Figure 40 and Figure 41, respectively.

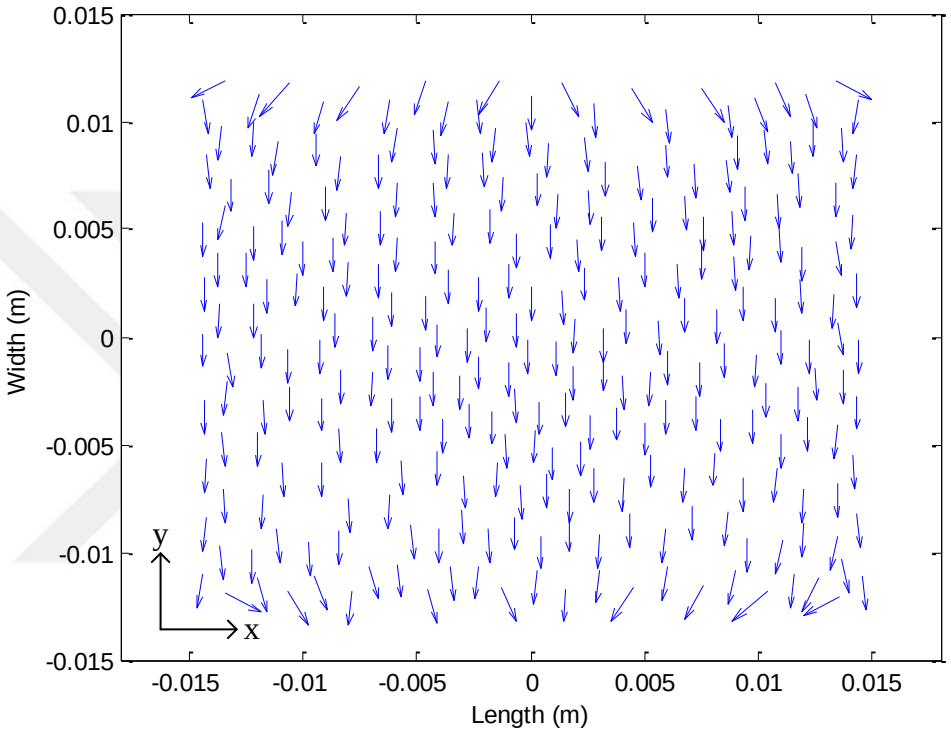

Figure 40 Current distribution of the 2nd mode obtained by code

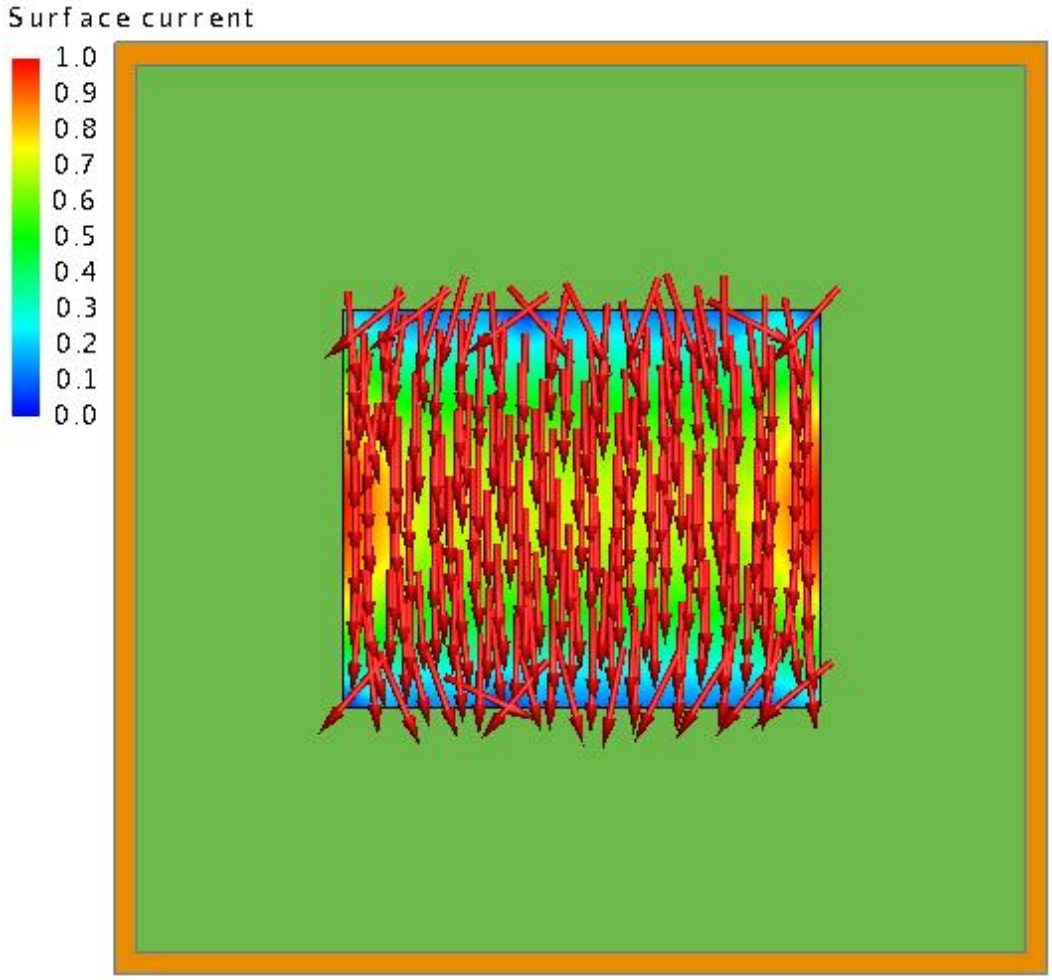

Figure 41 Current distribution of the 2nd mode obtained by FEKO

As shown in Figure 40 and Figure 41, currents are aligned in *y*-direction for the second mode. Therefore, this mode can be called as the vertical mode.

Since the horizontal dimension of the patch (30mm) is larger than its vertical dimension (25mm), the resonance of the horizontal mode occurs at a frequency (2.8 GHz) lower than that of the vertical mode (3.3 GHz). Moreover, the inverse proportionality relation between resonance length and resonance frequency holds.

$$\frac{30\ mm}{25\ mm} = 1.2 \qquad \frac{3.3\ GHz}{2.8\ GHz} = 1.18$$

3.3.2. Computation of the Input Admittance

The coaxial feeding is added to the antenna structure in this part. The rectangular microstrip patch antenna structure and the interested frequency band are the same as the previous part. Input admittances for two different feeding positions are computed by using the developed code and by using FEKO. The results obtained from the developed code and obtained from FEKO are compared and discussed.

The coaxial probe fed microstrip antenna is modeled in FEKO as shown in Figure 42. The input impedance is calculated at the surface where probe is connected to the ground plane.

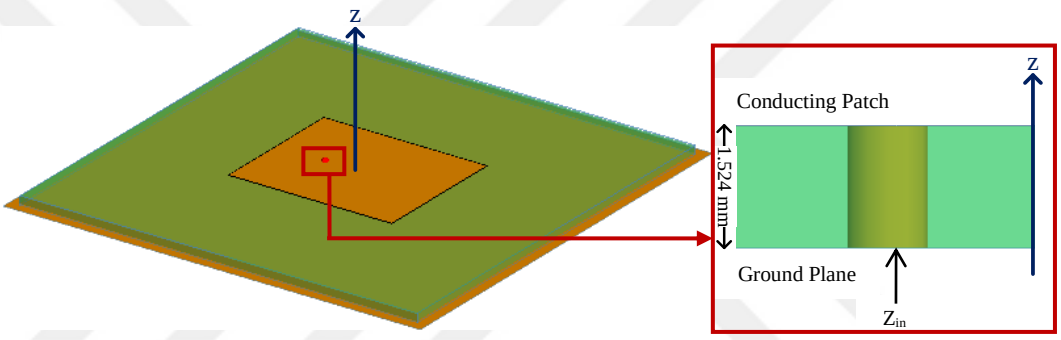

Figure 42 3D coaxial probe fed microstrip antenna model in FEKO

By using the developed code, the input impedance is computed by utilizing the feeding model explained in Chapter 2. Equation (2.68) is used with characteristic mode parameters in order to achieve the input impedance computation.

The antenna structure is placed on the *xy* plane and the center point of the rectangular patch is assumed to be (0, 0). The first feeding position is chosen as point (-6, 0). This feeding point is on the "*y = 0*" line and long edge of the antenna structure determines the resonance behavior at the interested frequency band. The real part, the imaginary part and the magnitude of input admittance obtained by using the developed code by comparison to FEKO results are presented in Figure 43, Figure 44 and Figure 45, respectively.

The second feeding position is chosen on the "*x = 0*" line as point (0, -6). In this case, short edge of the antenna structure determines the resonance behavior. The real part, the imaginary part and the magnitude of input admittance obtained by using the developed code by comparison to FEKO results are presented in Figure 46, Figure 47 and Figure 48, respectively.

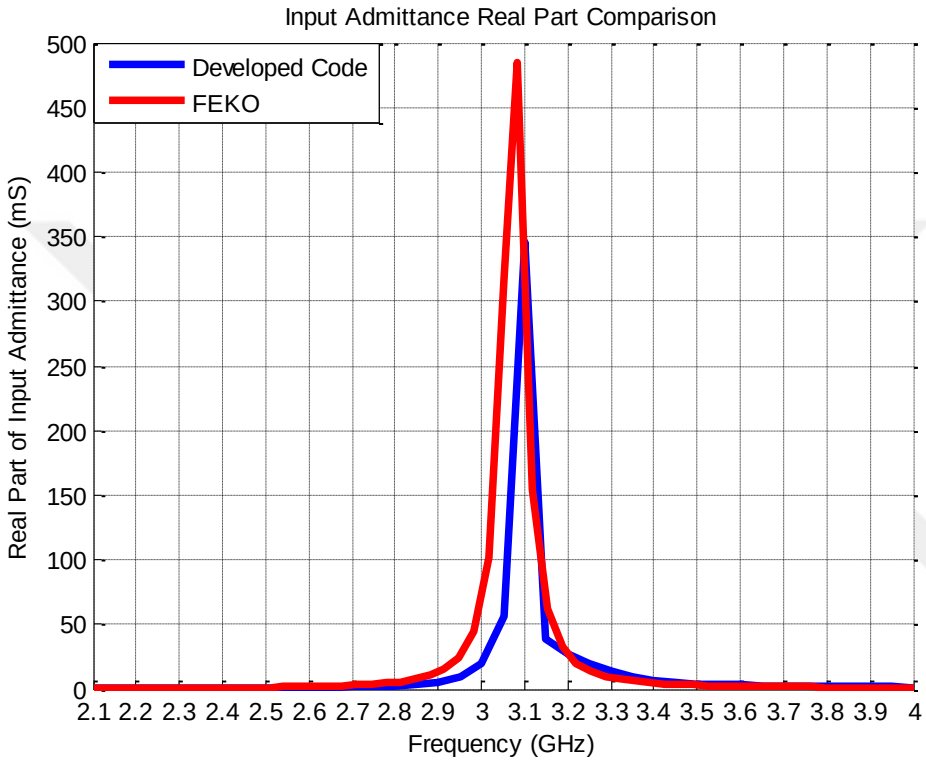

Figure 43 Real part of input admittance for the feed position (-6, 0)

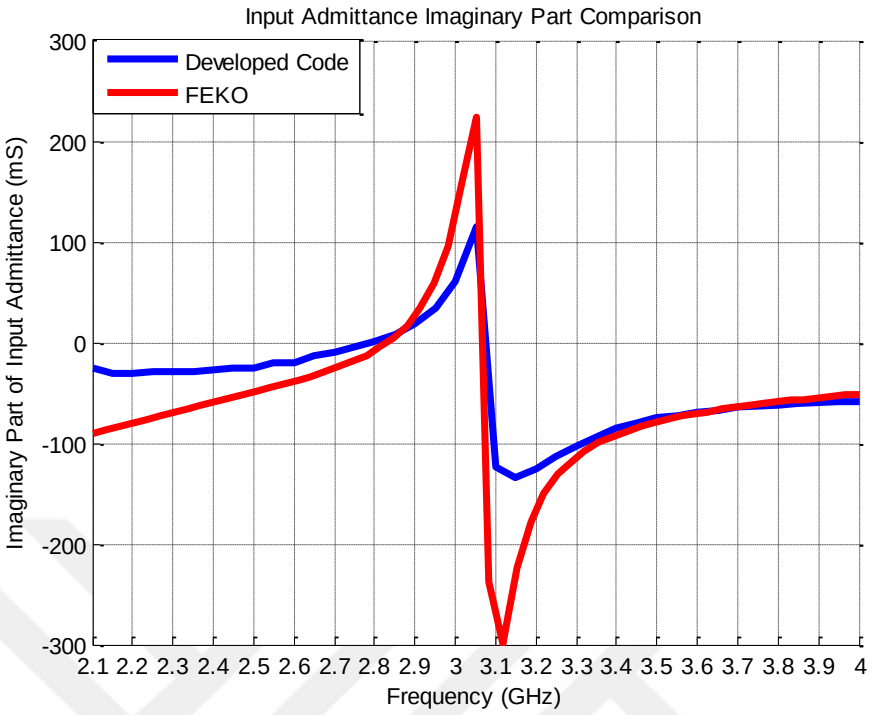

Figure 44 Imaginary part of input admittance for the feed position (-6, 0)

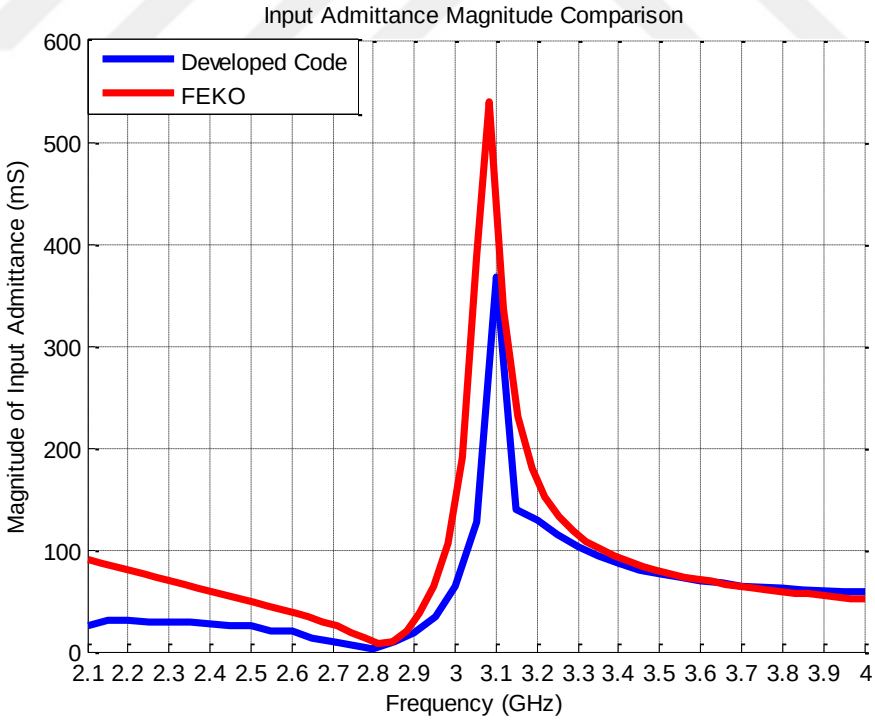

Figure 45 Magnitude of input admittance for the feed position (-6, 0)

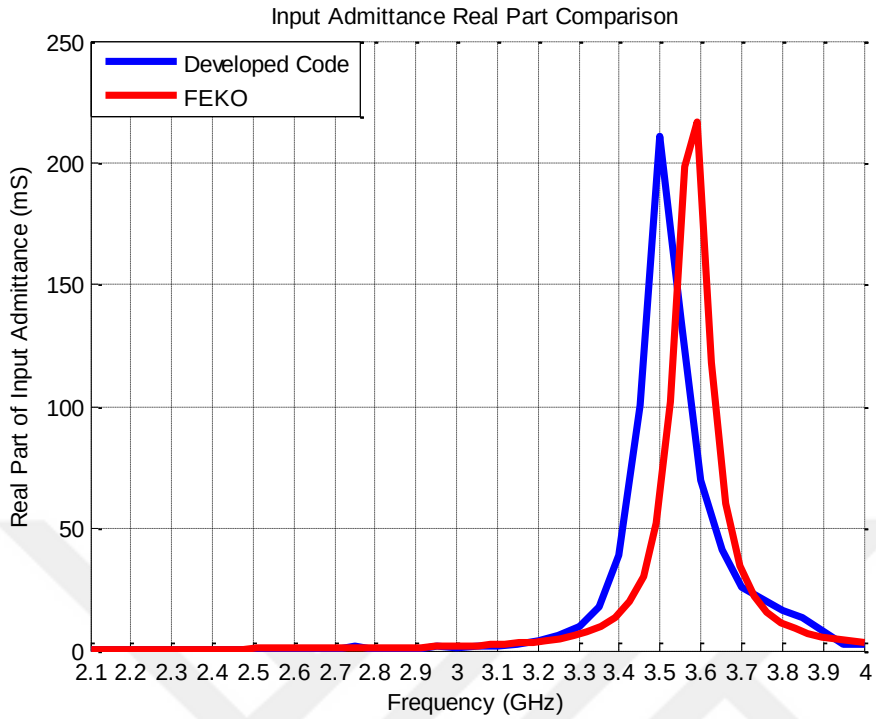

Figure 46 Real part of input admittance for the feed position (0, -6)

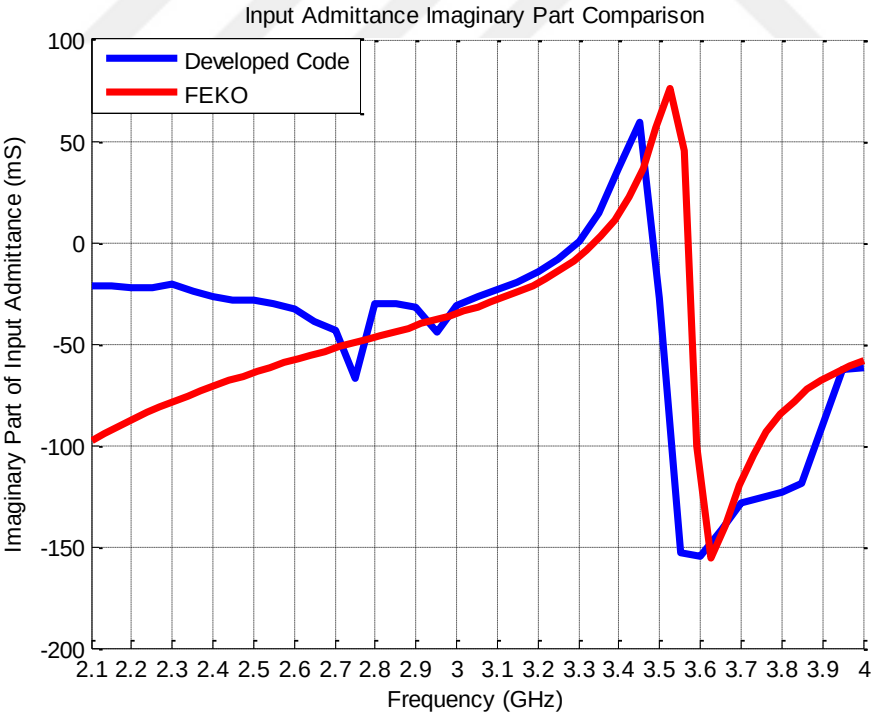

Figure 47 Imaginary part of input admittance for the feed position (0, -6)

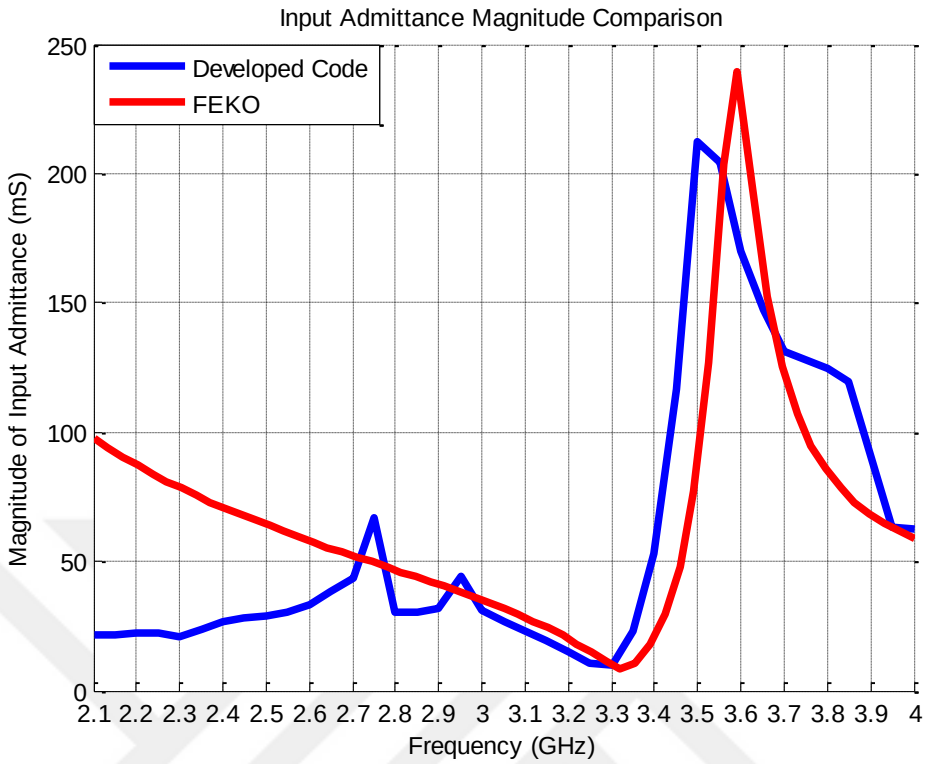

Figure 48 Magnitude of input admittance for the feed position (0, -6)

Although the computed input admittances for two feeding points by using the developed code sufficiently coincide with FEKO full-wave analysis results, there are small differences in resonance frequencies and amplitudes of the real part, the imaginary part and the magnitude of input admittances. The reasons of these errors are explained below.

One characteristic mode is not sufficient to compute input admittance, because the other characteristic modes affects input admittance significantly. Therefore, the number of characteristic modes is an important parameter for input admittance computation. However, the number of modes is chosen empirically and the first 9 modes are used to compute input admittance. In order to specify the number of modes that provides convergence of input admittance, a convergence algorithm should be added to the developed code. The real part of the input impedance is related to the power radiated by the antenna which is a far field parameter. Hence

second order errors affect the real part of the impedance. However, the imaginary part represents the stored energy in the near field of the antenna. Therefore, the higher order modes significantly affect the accurate computation of the imaginary part of the impedance.

The theory of characteristic modes and the coaxial feeding model used in this work involve some assumptions. These assumptions cause additional errors on input admittance computation. These errors may be minimized by improving the feeding model.

A last discussion will be about the modal excitation coefficients for different feed locations.

Table 3 Modal significances and modal excitation coefficients of the modes

Frequency	Parameter	The First Mode	The Second Mode
2.8 GHz	**MS**	0.9153	0.0408
	V_n^i for (-6, 0)	2.05×10^{-6} $- j6.13 \times 10^{-4}$	7.22×10^{-8} $- j2.47 \times 10^{-5}$
	V_n^i for (0, -6)	$- 4.69 \times 10^{-8}$ $+ j2.28 \times 10^{-5}$	$- 1.94 \times 10^{-6}$ $+ j7.56 \times 10^{-4}$
3.3 GHz	**MS**	0.0862	0.9692
	V_n^i for (-6, 0)	3.96×10^{-6} $- j5.43 \times 10^{-4}$	1.43×10^{-7} $- j1.97 \times 10^{-5}$
	V_n^i for (0, -6)	$- 8.97 \times 10^{-8}$ $+ j2.29 \times 10^{-5}$	$- 3.76 \times 10^{-6}$ $+ j6.61 \times 10^{-4}$

As shown in Table 3, the first mode is the dominant mode according to MS values at 2.8 GHz which is the resonance frequency of the first mode. For the feed position on the "*y = 0*" line (-6, 0), absolute value of the real part and the imaginary part of modal excitation coefficient of the first mode are greater than the second mode, hence the first mode is excited stronger than the second mode. However, for the feed position on the "*x = 0*" line (0, -6), value of the same

parameter of the second mode are greater than the first mode, in spite of the first mode is the dominant mode according to MS values. It means, the first mode can not be excited strongly for the feed position (0, -6) even if its MS value is greater than the second mode. At 3.3 GHz which is the resonance frequency of the second mode, according to MS values the second mode is the dominant mode. Although the MS value of the second mode greater than the first mode, for the feed position (-6, 0), the second mode can not be excited strongly, since absolute value of the real part and the imaginary part of modal excitation coefficient of the first mode are greater than the second mode. For the feed position (0, -6), the second mode is excited stronger than the first mode according to both MS values and modal excitation coefficients. These results are expected with regard to antenna theory, since excitation of the vertical mode (the second mode) is not expected by feeding the rectangular patch antenna from points on the "$y = 0$" line. Similarly, excitation of the horizontal mode (the first mode) is not expected by feeding the rectangular patch antenna from points on the "$x = 0$" line.

It is obvious that characteristic mode analysis of this type of structures by using the developed code can provide antenna designer an acceptable starting point before optimization.

CHAPTER 4

CONCLUSION AND FUTURE WORK

In this thesis, a code is developed in MATLAB to analyze characteristic modes of printed structures. Characteristic mode analysis is made to the rectangular conducting patch, an ultra wide band printed planar bevel-shaped quasi-monopole antenna and rectangular microstrip patch antenna.

Developments in RF based systems enforce microwave engineers to design wide band antennas. Electromagnetic simulators are needed to obtain this, because an analytical method does not exist for complicated antenna geometries. However, as a result of using electromagnetic simulators, the physical insight for radiating behavior of an antenna is overlooked. This problem may be eliminated for antenna design by using the theory of characteristic modes efficiently.

The theory of characteristic modes brings physical insight for radiating behavior of antenna structures. Characteristic mode analysis of an antenna can be interpreted as a good starting point for the optimization of antenna parameters. As a result, the number of iterations in the optimization cycle is reduced. Characteristic modes are useful for antenna design, due to the sufficiency of a few modes to understand scattering phenomena of a conducting surface and the orthogonality property of the modes. Two important steps of antenna design, shape and size optimization and selecting the optimum feeding configuration, can be achieved by using characteristic modes. Because characteristic modes only depend on the shape and size of conducting surface, they do not depend on excitation. By considering the possible excited modes, shape and size can be

optimized. The feeding configuration for intended modes to be excited can be selected by using characteristic modes.

In this work, first of all, development of the code which is used to analyze characteristic modes of printed structures, is completed in MATLAB. To test the code, scattering analysis and characteristic mode analysis of a rectangular conducting patch of length 6 cm and width 4 cm is made at 2.4 GHz. The comparison of the results with the results presented in [5] verified the accuracy of the developed code for structures with simple shapes.

After this verification, characteristic mode analysis is made to the ultra wide band printed planar bevel-shaped quasi-monopole antenna structure by using the commercial electromagnetic simulator FEKO and by using the developed code at 3-11 GHz frequency band. The comparison of the results showed that the developed code can be used in the analysis of arbitrarily shaped, more complex structures.

Finally, characteristic modes analysis and input impedance computation for different feeding points are made to the rectangular microstrip patch antenna structure by using the developed code and by using FEKO. These studies are made at 2-3.9 GHz frequency band which involves the resonance frequencies of the first and the second characteristic modes. As a result, it is shown that characteristic mode analysis and input impedance computation can be made by using the developed code for simple printed structures.

4.1. Future Studies

For future work, the coaxial feeding model may be improved by using junction basis functions proposed in [49] and computation of the input impedance can be made more accurately. It is important to specify the number of characteristic modes which are taken into consideration for the computation of input impedance. An algorithm which specifies the number of modes that provides convergence of

input impedance may be added to the developed code. Mode tracking, which is the extraction of the modes within a wide frequency bandwidth without the need of eigenvalue computation at discrete frequencies sampled in the bandwidth, is another important research subject [50, 51]. A mode tracking algorithm can be developed. Thus, characteristic mode analysis and input impedance computation can be made more accurately and more efficiently for the microstrip patch antenna structures by using the developed code. After these improvements, the developed code may be used to analyze the microstrip patch antenna structures with different dielectric substrates, different substrate thicknesses and different geometries such as patches with slots.

REFERENCES

[1] "User Manual for HFSS," Ansoft Corporation, Pittsburg, PA, USA.

[2] "FEKO User's Manual," Suite 7.0, EM Software & Systems, South Africa, May 2014.

[3] "CST Microwave Studio 2016 - Workflow and Solver Overview," CST - Computer Simulation Technology AG, Germany.

[4] Fabres, M. C., Daviu, E. A., Nogueira, A. V., and Bataller, M. F., "The Theory of Characteristic Modes Revisited: A Contribution to the Design of Antennas for Modern Applications," IEEE Antennas and Propagation Magazine, Vol. 49, No. 5, pp. 52–68, October 2007.

[5] Fabres, M. C., "Systematic Design of Antennas Using the Theory of Characteristic Modes," Ph. D. dissertation, Polytechnic University of Valencia, February 2007.

[6] Garbacz, R. J., "A Generalized Expansion of Radiated and Scattered Fields," Ph. D. dissertation, Ohio State University, Columbus, 1968.

[7] Garbacz, R. J., and Turpin, R. H., "A Generalized Expansion of Radiated and Scattered Fields," IEEE Transactions on Antennas and Propagation, Vol. AP-19, No. 3, pp. 348-358, May 1971.

[8] Turpin, R. H., "Basis Transformation, Least Square, and Characteristic Mode Techniques for Thin-Wire Scattering Analysis," Ph. D. dissertation, Ohio State University, Columbus, 1970.

[9] Garbacz, R. J., and Wickliff, R., "Introduction to Characteristic Modes for Chaff Applications," Air Force Avionics Lab., Wright-Patterson A. F. B., Ohio, Contract F33615-68-C-1252, Tech. Rep. 2584-6.

[10] Harrington, R. F., "Field Computation by Moment Method," Macmillan, New York, 1968.

[11] Harrington, R. F., and Mautz, J. R., "Theory of Characteristic Modes for Conducting Bodies," IEEE Transactions on Antennas and Propagation, Vol. AP-19, No. 5, pp. 622-628, September 1971.

[12] Harrington, R. F., and Mautz, J. R., "Computation of Characteristic Modes for Conducting Bodies," IEEE Transactions on Antennas and Propagation, Vol. AP-19, No. 5, pp. 629-639, September 1971.

[13] Garbacz, R. J., and Pozar, D. M., "Antenna Shape Synthesis Using Characteristic Modes," IEEE Transactions on Antennas and Propagation, Vol. AP-30, No. 3, pp. 340-350, May 1982.

[14] Yang, B., and Adams, J. J., "Systematic Shape Optimization of Symmetric MIMO Antennas Using Characteristic Modes", IEEE Transactions on Antennas and Propagation, Vol. 64, No. 7, pp. 2668-2678, July 2016.

[15] Ethier, J., Lanoue, E., and McNamara, D., "MIMO Handheld Antenna Design Approach Using Characteristic Mode Concepts", Microwave and Optical Technology Letters, Vol. 50, No. 7, pp. 1724-1727, November 2007.

[16] Ethier, J., and McNamara, D. A., "The Use of Generalized Characteristic Modes in the Design of MIMO Antennas", IEEE Transactions on Magnetics, Vol. 45, No. 3, pp. 1124-1127, March 2009.

[17] Bouezzeddine, M., and Schroeder, W. L., "Design of a Wideband, Tunable Four-Port MIMO Antenna System With High Isolation Based on the Theory of Characteristic Modes", IEEE Transactions on Antennas and Propagation, Vol. 64, No. 7, pp. 2679-2688, July 2016.

[18] Li, H., Miers, Z. T., and Lau, B. K., "Design of Orthogonal MIMO Handset Antennas Based on Characteristic Mode Manipulation at Frequency Bands Below

1 GHz", IEEE Transactions on Antennas and Propagation, Vol. 62, No. 5, pp. 2756-2766, May 2014.

[19] Miers, Z., Li, H., and Lau, B. K., "Design of Bandwidth-Enhanced and Multiband MIMO Antennas Using Characteristic Modes", IEEE Antennas and Wireless Propagation Letters, Vol. 12, pp. 1696-1699, 2013.

[20] Deng, C., Feng, Z., and Hum, S. V., "MIMO Mobile Handset Antenna Merging Characteristic Modes for Increased Bandwidth", IEEE Transactions on Antennas and Propagation, Vol. 64, No. 7, pp. 2660-2667, July 2016.

[21] Manteuffel, D., and Martens, R., "Compact Multimode Multielement Antenna for Indoor UWB Massive MIMO", IEEE Transactions on Antennas and Propagation, Vol. 64, No. 7, pp. 2689-2697, July 2016.

[22] Araghi, A., and Dadashzadeh, G., "Oriented Design of an Antenna for MIMO Applications Using Theory of Characteristic Modes", IEEE Antennas and Wireless Propagation Letters, Vol. 11, pp. 1040-1043, 2012.

[23] Shih, T., and Behdad, N., "Bandwidth Enhancement of Platform-Mounted HF Antennas Using the Characteristic Mode Theory", IEEE Transactions on Antennas and Propagation, Vol. 64, No. 7, pp. 2648-2659, July 2016.

[24] Chen, Y., and Wang, C., "Electrically Small UAV Antenna Design Using Characteristic Modes", IEEE Transactions on Antennas and Propagation, Vol. 62, No. 2, pp. 535-545, February 2014.

[25] Chen, Y., and Wang, C., "HF Band Shipboard Antenna Design Using Characteristic Modes", IEEE Transactions on Antennas and Propagation, Vol. 63, No. 3, pp. 1004-1013, March 2015.

[26] Obeidat, K. A., Raines, B. D., and Rojas, R. G., "Application of Characteristic Modes and Non-Foster Multiport Loading to the Design of Broadband Antennas", IEEE Transactions on Antennas and Propagation, Vol. 58, No. 1, pp. 203-207, January 2010.

[27] Obeidat, K. A., Raines, B. D., Rojas, R. G., and Strojny, B. T., “Design of Frequency Reconfigurable Antennas Using the Theory of Characteristic Modes”, IEEE Transactions on Antennas and Propagation, Vol. 58, No. 10, pp. 3106-3113, October 2010.

[28] Chen, Y., and Wang, C., “Synthesis of Reactively Controlled Antenna Arrays Using Characteristic Modes and DE Algorithm”, IEEE Antennas and Wireless Propagation Letters, Vol. 11, pp. 385-388, 2012.

[29] Martens, R., and Manteuffel, D., "Systematic Design Method of a Mobile Multiple Antenna System Using the Theory of Characteristic Modes," IET Microwaves, Antennas & Propagation, Vol. 8, No. 12, pp. 887-893, September 2014.

[30] Elghannai, E. A., and Rojas, R. G., "Design of USB Dongle Antenna for WLAN Applications Using Theory of Characteristic Modes," Electronics Letters, Vol. 50, No. 4, pp. 249-251, February 2014.

[31] Gallee, F., Bernabeu, T., Fabres, M. C., Daviu, E. A., Nogueira, A. V., "Application of the Theory of Characteristic Modes to the Design of Compact Metallic Strip Antenna with Multilayer Technology (LTCC)," The 7th European Conference on Antennas and Propagation (EuCAP 2013), Gothenburg, pp. 1891-1895, April 2013.

[32] Erçil, E., Alatan, L., and Civi, Ö. A., “An Efficient Numerical Solution Method for Reflectarrays of Varying Element Sizes”, IEEE Transactions on Antennas and Propagation, Vol. 63, No. 12, pp. 5668-5676, December 2015.

[33] "MATLAB Primer," The Math Works Inc., Natick, MA, USA, September 2015.

[34] Rao, S. M., Wilton, D. R., and Glisson, A. W., "Electromagnetic Scattering by Surfaces of Arbitrary Shape," IEEE Transactions on Antennas and Propagation, Vol. AP-30, No. 3, pp. 409-418, May 1982.

[35] "Partial Differential Equation Toolbox User's Guide," The Math Works Inc., Natick, MA, USA, September 2015.

[36] Geuzaine, C, and Remacle, J. F., "Gmsh: a three-dimensional finite element mesh generator with built-in pre- and post-processing facilities," International Journal for Numerical Methods in Engineering, 79(11), pp. 1309-1331, 2009.

[37] Fang, D. G., Yang, J. J., and Delisle, G. Y., "Discrete Image Theory for Horizontal Electric Dipoles in a Multilayered Medium", IEE Proceedings H - Microwaves, Antennas and Propagation, Vol. 135, No. 5, pp. 297-303, October 1988.

[38] Aksun, M. I., "A Robust Approach for the Derivation of Closed-Form Green's Functions," IEEE Transactions on Microwave Theory and Techniques, Vol. 44, No. 5, pp. 651-658, May 1996.

[39] Alparslan, A., Aksun, M. I., and Michalski, K. A., "Closed-Form Green's Functions in Planar Layered Media for All Ranges and Materials," IEEE Transactions on Microwave Theory and Techniques, Vol. 58, No. 3, pp. 602-613, March 2010.

[40] Karabulut, E. P., Erdogan, A. T., and Aksun, M. I., "Discrete Complex Image Method With Spatial Error Criterion", IEEE Transactions on Microwave Theory and Techniques, Vol. 59, No. 4, pp. 793-802, April 2011.

[41] Makarov, S. N., "Antenna and EM Modeling with MATLAB," Wiley-Interscience, John Wiley & Sons, New York, July 2002.

[42] Harrington, R. F., "Time-Harmonic Electromagnetic Fields," McGraw-Hill, New York, 1961.

[43] Austin, B. A., and Murray, K. P. "The Application of Characteristic-Mode Techniques to Vehicle-Mounted NVIS Antennas," IEEE Antennas and Propagation Magazine, Vol. 40, No. 1, pp. 7-21, February 1998.

[44] Kamen, Y., and Shirman, L., "Triangle Rendering Using Adaptive Subdivision," IEEE Computer Graphics and Applications, Vol. 18, No. 2, pp. 95-105, March-April 1998.

[45] Daviu, E. A., Fabres, M. C., Bataller, M. F., and Penarrocha, V. M. R., "Modal Analysis and Design of Band-Notched UWB Planar Monopole Antennas", IEEE Transactions on Antennas and Propagation, Vol. 58, No. 5, pp. 1457-1467, May 2010.

[46] Pozar, D. M., "Input Impedance and Mutual Coupling of Rectangular Microstrip Antennas", IEEE Transactions on Antennas and Propagation, Vol. AP-30, No. 6, pp. 1191-1196, November 1982.

[47] Wu, W., and Zhang, Y. P., "Analysis of Ultra-Wideband Printed Planar Quasi-Monopole Antennas Using the Theory of Characteristic Modes," IEEE Antennas and Propagation Magazine, Vol. 52, No. 6, pp. 67-77, December 2010.

[48] "RT/duroid 6002 High Frequency Laminates Data Sheet", Rogers Corporation, Chandler, AZ, USA.

[49] Champagne, N. J., Johnson, W. A., and Wilton, D. R., "On Attaching a Wire to a Triangulated Surface", IEEE Antennas and Propagation Society Symposium, San Antonio, TX, June 16-21, 2002.

[50] Safin, E., Manteuffel, D., "Advanced Eigenvalue Tracking of Characteristic Modes", IEEE Transactions on Antennas and Propagation, Vol. 64, No. 7, pp. 2628-2636, July 2016.

[51] Schab, K. R., Outwater, J. M., Young, M. W., Bernhard, J. T., "Eigenvalue Crossing Avoidance in Characteristic Modes", IEEE Transactions on Antennas and Propagation, Vol. 64, No. 7, pp. 2617-2627, July 2016.